Supporting Information

Electronically Tunable Perfect Absorption in Graphene

Seyoon Kim[†,+], Min Seok Jang[†,‡,+], Victor W. Brar[†,§,∥,+], Kelly W. Mauser[†], Laura Kim[†], and Harry A. Atwater[†,§,*]

[*]haa@caltech.edu

[+]Equally contributed authors

[†]Thomas J. Watson Laboratory of Applied Physics, California Institute of Technology, Pasadena, California 91125, United States

[‡]School of Electrical Engineering, Korea Advanced Institute of Science and Technology, Daejeon 34141, Republic of Korea

[§]Kavli Nanoscience Institute, California Institute of Technology, Pasadena, CA 91125, United States

[∥]Department of Physics, University of Wisconsin-Madison, Madison, Wisconsin 53711, United States

Contents

1. Electric field enhancement by Salisbury screen

To enhance absorption in graphene plasmonic ribbons (GPRs), we exploited the field enhancement in the GPRs via a Salisbury screen consisting of a dielectric stack and a back reflector[1-3]. Since the field enhancement at the interface between the air and the dielectric stack is a result of the interference between the incoming light and the reflected light from the back reflector, the electric field intensity at the interface could be larger or smaller than the incoming light depending on the wavelength and the dielectric stack thickness. When the thickness of the dielectric stack matches to the quarter wavelength resonance condition, the electric field intensity is maximized at the interface because the phase shift of the reflected radiation at the back reflector is π, which leads to constructive interference at the air/dielectric stack interface. Theoretical maximum enhancement is a factor of 4, and the maximum achievable enhancement factor decreases with absorption in the dielectric stack and the back reflector.

Figure S1a,b shows the electric field intensity enhancement on the SiN_x 1.05 μm/Au and the SiO_2 150 nm/SiN_x 1 μm/Au Salisbury screens. Both Salisbury screens are optimized to maximize the electric field intensity at 1356 cm^{-1} on the air/dielectric interface (z=0), and the maximum electric field intensity enhancements on the SiN_x on the SiO_2 are 3.76 and 3.77 at 1356 cm^{-1}, respectively.

Figure S1c,d shows the absorption in the GPRs by the field enhancement depending on the substrate thickness at 1356 cm^{-1}. The electric field at the air/dielectric interface exhibit resonance depending on the SiN_x thickness, and the maxima and the minima occur at $d_{\mathrm{sub}} \approx \frac{\lambda_0}{4n_{\mathrm{sub}}}$ and $d_{\mathrm{sub}} \approx \frac{\lambda_0}{2n_{\mathrm{sub}}}$, respectively ($\lambda_0$: free-space wavelength, d_{sub}: substrate thickness, n_{sub}: effective refractive index of substrate). As a result of the standing wave resonance in the substrate, the absorption in the GPRs follows the field enhancement profiles. The near-fields around the GPRs also increase or decrease depending on the field enhancement, as shown in Figure S1e-h.

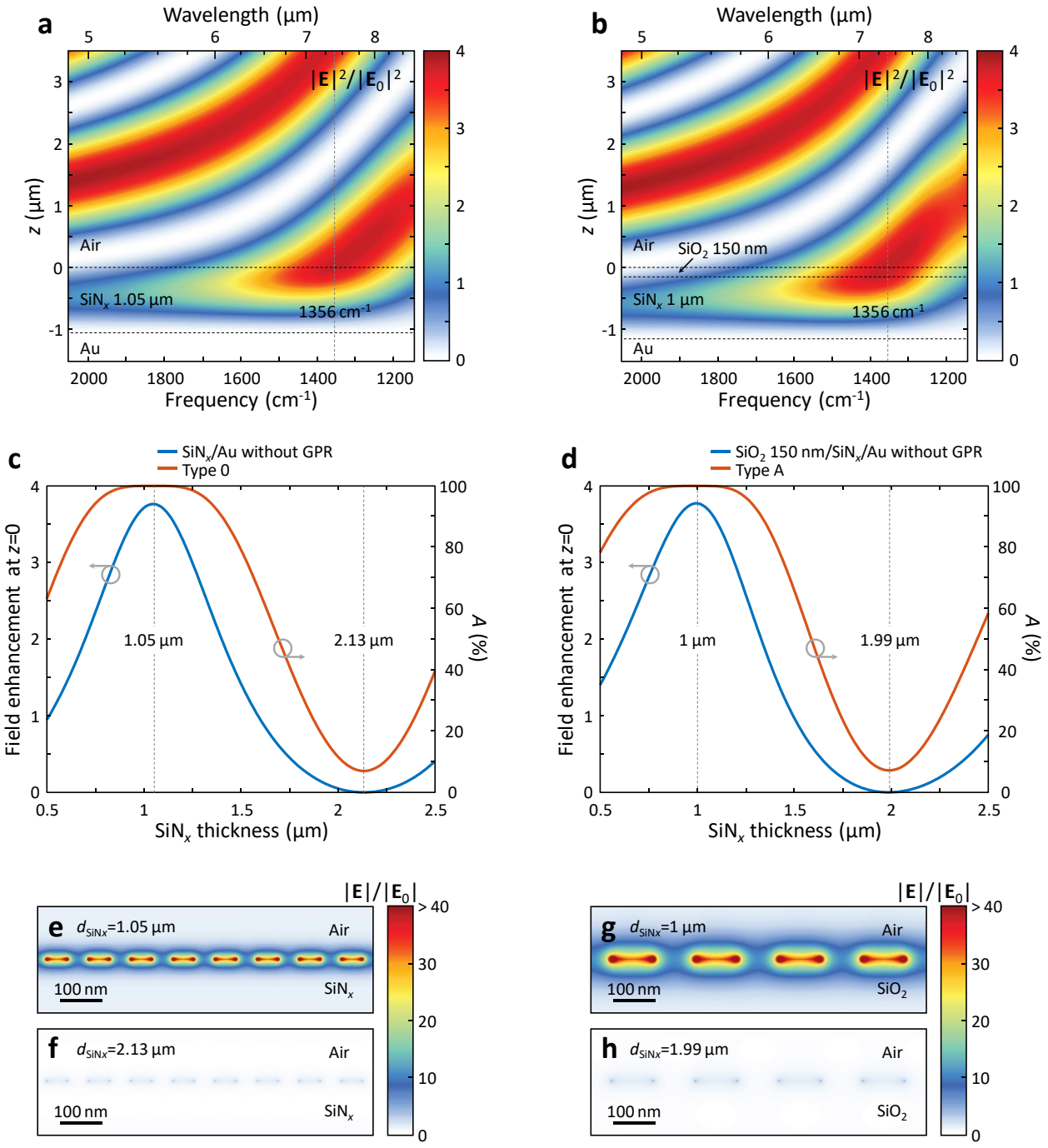

Figure S1. Field enhancement as a function of frequency (a) on a SiN_x 1.05 μm/Au substrate and (b) on a SiO_2 150 nm/SiN_x 1 μm/Au substrate. Absorptions (c) in the type 0 structure and (d) in the type A structure at 1356 cm^{-1} as a function of SiN_x thickness (d_{SiNx}). Electric field distributions (e) at the maximum absorption and (f) at the minimum absorption in the type 0 structures. Electric field distributions (g) at the maximum absorption and (h) at the minimum absorption in the type A structures.

2. Electric field profiles with varying graphene carrier mobilities

The oscillator strength in the GPRs is strongly dependent on graphene carrier mobility. Stronger oscillation is induced for higher graphene carrier mobility as shown in the electric field and electric intensity distributions in Figure S2. In all structures, the near fields are strongly enhanced around the GPRs with higher graphene carrier mobility. However, stronger oscillation does not always result in a larger absorption in these structures. There exists an optimal graphene carrier mobility to achieve perfect absorption in each structure, and it can be explained with a surface admittance model as discussed in Supporting Information Part 7.

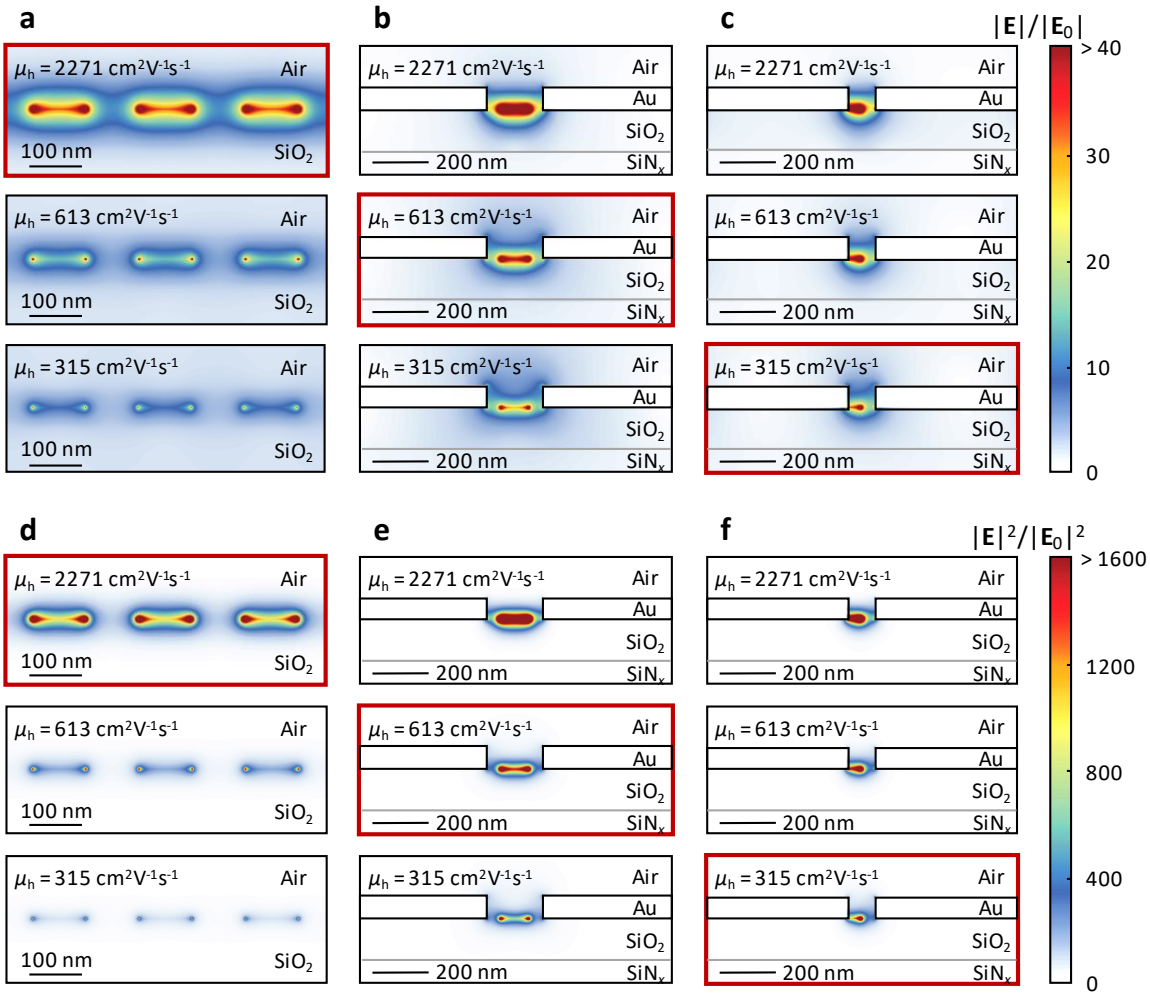

Figure S2. (a-c) Electric field ($|\mathbf{E}|/|\mathbf{E}_0|$) distributions in the type A, B, and C structure, respectively, with different graphene carrier mobilities. (d-f) Electric field intensity ($|\mathbf{E}|^2/|\mathbf{E}_0|^2$) distributions in the type A, B, and C structures, respectively, with different graphene carrier mobilities. Field profiles with red boxes correspond to the perfect absorption conditions in the structures.

3. Graphene plasmonic ribbons on a low permittivity substrate

The dispersion relation of a transverse magnetic graphene plasmons in the quasi-static regime can be approximated by[4-6]:

$$k_{\mathrm{p}} = \varepsilon_0(1+\varepsilon_{\mathrm{sub}})\frac{i\omega}{\sigma} \qquad \text{(S1)}$$

where $\varepsilon_{\mathrm{sub}}$ is the substrate relative permittivity, and σ is the optical surface conductivity of graphene[7,8]. The dispersion relation in eq S1 implies that graphene plasmons will have a relatively smaller wavenumber on a low permittivity substrate, thus reducing the wavevector mismatch between free-space photons and graphene plasmons, resulting in higher coupling efficiency.

Figure S3a shows the relative permittivities of SiO_2 and SiN_x indicating that SiO_2 has lower permittivity than SiN_x. The dispersion relation of graphene plasmons at 1356 cm^{-1} for each Salisbury screen is calculated in Figure S3b as a function of graphene Fermi level (E_F). Since SiO_2 has a lower permittivity than SiN_x, the graphene plasmon on SiO_2 exhibits a smaller wavenumber (or longer wavelength) than on SiN_x. The normalized wavenumber (k_p/k_0) of graphene plasmon on SiO_2/SiN_x/Au is 24.2+i0.91 with E_F=-0.484 eV, and this wavenumber is nearly half of the graphene plasmon wavenumber on SiN_x/Au, where the normalized wavenumber is 48.1+i1.82 with the same graphene Fermi level. Here, the graphene plasmon on SiO_2 exhibits negligible coupling to the bottom SiN_x because the skin depth in the substrate (δ_2=48.2 nm) is smaller than the SiO_2 thickness (150 nm), as shown in Figure S3c. In addition, the graphene plasmon on SiO_2 has a smaller confinement factor than on the SiN_x. As a result, the graphene plasmon on SiO_2 has a smaller decay rate, and it can propagate a greater distance than on SiN_x, as shown in Figure S3d,e.

Using the dispersion relation of graphene plasmons as a guide, we find that wider GPRs can be used on a SiO_2/SiN_x/Au substrate as compared to a SiN_x/Au substrate for a desired resonance frequency. Figure S3f shows the absorption at 1356 cm^{-1} on each Salisbury screen structure as a function of ribbon width and gap width with E_F=-0.484 eV. If we cut along the 1:1 of ribbon:gap ratio line, which ensures the same graphene coverage for both structures, we find that absorption is maximized for 50.2 nm/50.2 nm and 100 nm/100 nm of ribbon/gap width GPRs for the type 0 and A structures, respectively. Since the wavevector mismatch is reduced on a low permittivity substrate, the type A structure induces a stronger resonance than the type 0 structure.

In addition to lowering the graphene carrier mobility required to achieve perfect absorption, use of SiO_2 to reduce wavevector mismatch via a low permittivity substrate is also beneficial in fabrication. Due to fabrication imperfections, edge roughness is inevitable in fabricated GPRs, and the resulting variation in ribbon/gap widths induces an inhomogeneous broadening of the absorption spectrum, which lowers the effective graphene carrier mobility. To estimate the effect of the edge roughness on absorption, we performed simple calculations assuming ±2 nm variations in the ribbon width, as shown below in Figure S4. In these calculations, the pitches of GPRs are fixed at 100.4 nm and 200 nm for the type 0 and A structures, respectively, and the ribbon widths are adjusted by ±2 nm with a 1 nm step from their optimized ribbon widths (50.2 nm for the type 0 structure and 100 nm for the type A structure). The graphene Fermi level and the graphene carrier mobility are assumed to show perfect

absorption in each structure with zero variation at 1356 cm^{-1}. Figure S4 shows two important results concerning ribbon width variation in the type 0 and A structures. First, the peak frequency shift is smaller in the type A structure (13 cm^{-1} from 1350 cm^{-1} to 1363 cm^{-1}) than in the type 0 structure (41 cm^{-1} from 1336 cm^{-1} to 1377 cm^{-1}) with variation in ribbon width. Second, the averaged maximum absorption is higher in the type A structure (95.2%) compared with the type 0 structure (85.1%). These simulation results clearly indicate that reducing the wavevector mismatch via a low permittivity substrate is helpful for making the fabricated samples robust to fabrication imperfections which cause inhomogeneous broadening.

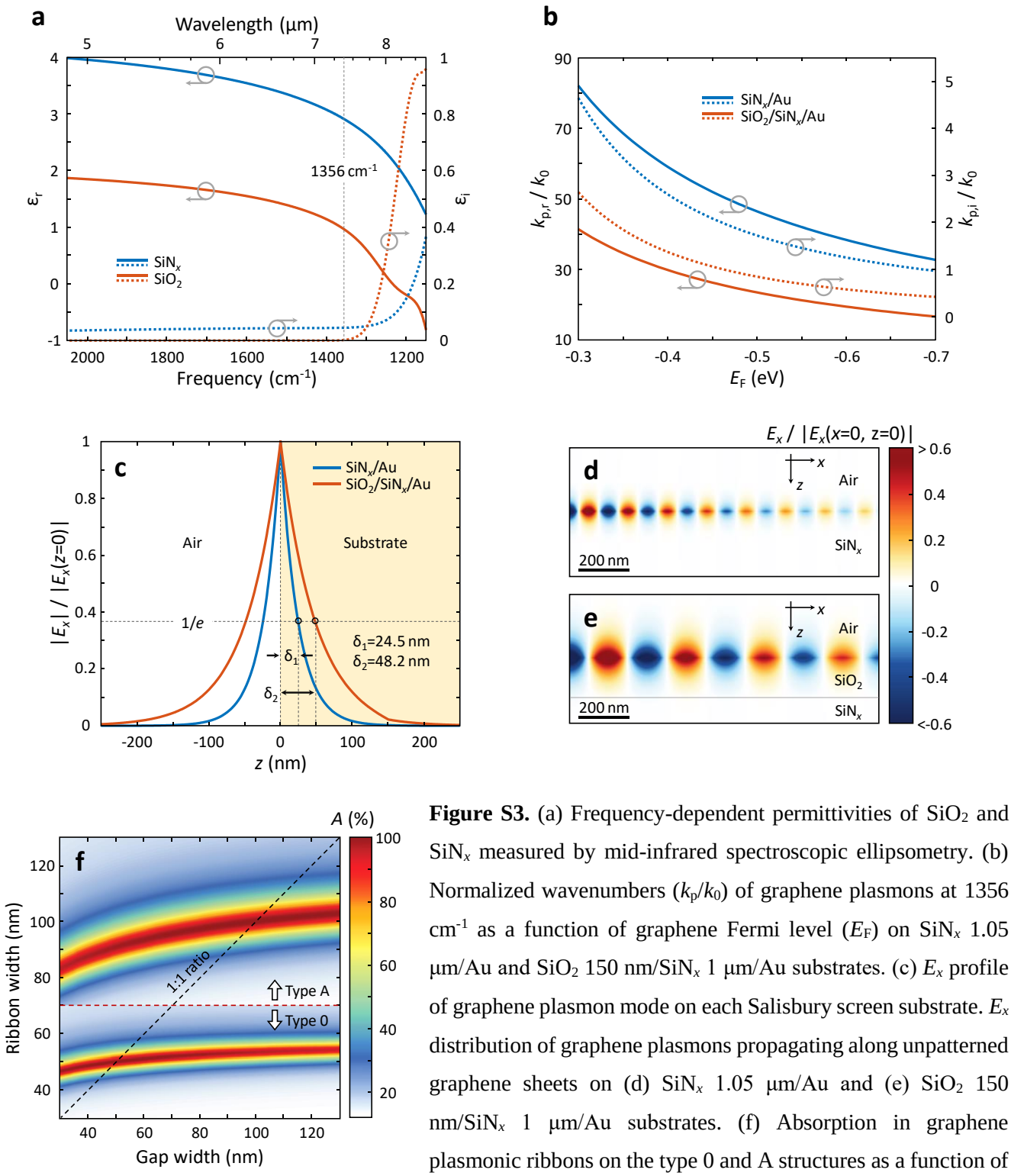

Figure S3. (a) Frequency-dependent permittivities of SiO_2 and SiN_x measured by mid-infrared spectroscopic ellipsometry. (b) Normalized wavenumbers (k_p/k_0) of graphene plasmons at 1356 cm^{-1} as a function of graphene Fermi level (E_F) on SiN_x 1.05 μm/Au and SiO_2 150 nm/SiN_x 1 μm/Au substrates. (c) E_x profile of graphene plasmon mode on each Salisbury screen substrate. E_x distribution of graphene plasmons propagating along unpatterned graphene sheets on (d) SiN_x 1.05 μm/Au and (e) SiO_2 150 nm/SiN_x 1 μm/Au substrates. (f) Absorption in graphene plasmonic ribbons on the type 0 and A structures as a function of ribbon width and gap width at 1356 cm^{-1} with E_F=-0.484 eV. In (b)-(f), graphene carrier mobilities on the SiO_2 150 nm/SiN_x 1 μm/Au substrate and the SiN_x 1.05 μm/Au substrate are assumed by 2271 $cm^2V^{-1}s^{-1}$ and 3174 $cm^2V^{-1}s^{-1}$, respectively.

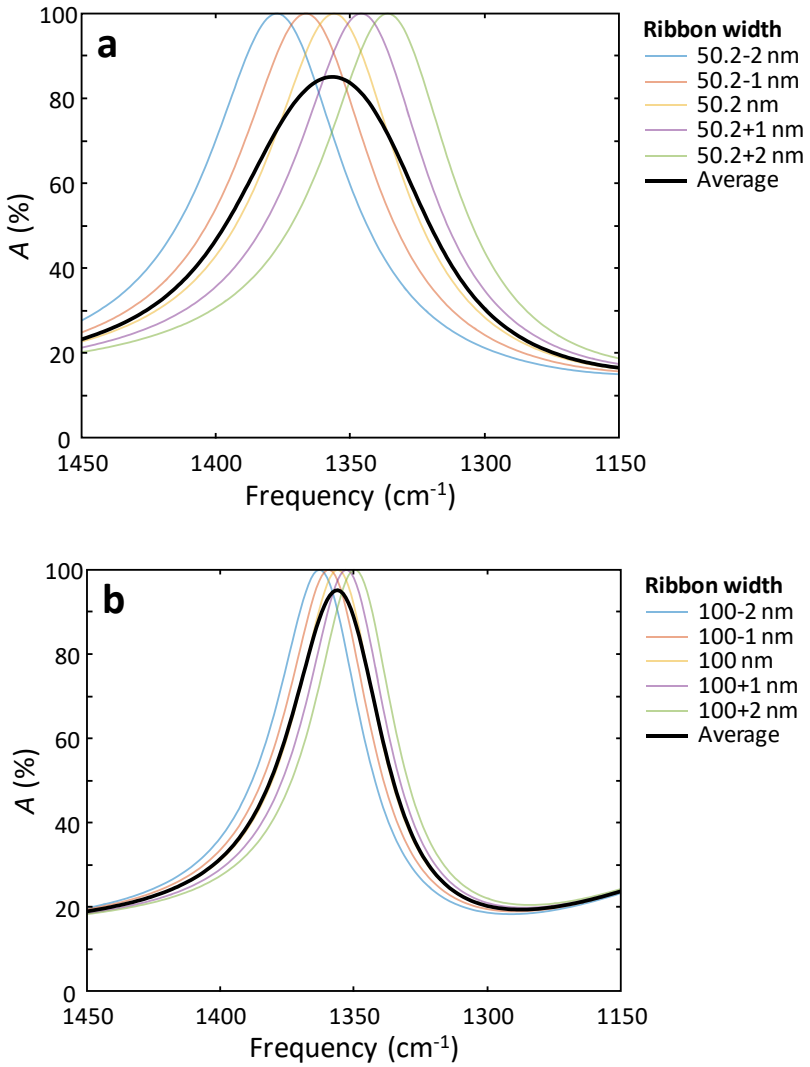

Figure S4. (a) Absorption spectra in the type 0 structure with different ribbon/gap widths. The pitch is fixed at 100.4 nm, and the ribbon width is adjusted by ±2 nm in 1 nm steps from 50.2 nm. The graphene carrier mobility and the graphene Fermi level are assumed to be 3174 cm^{-1} and -0.484 eV, respectively, where perfect absorption is achieved with a ribbon width of 50.2 nm. The peak frequency shifts by 41 cm^{-1} from 1336 cm^{-1} to 1377 cm^{-1}. The maximum average absorption is 85.1% at 1356 cm^{-1}. (b) Absorption spectra in the type A structure with different ribbon/gap widths. The pitch is fixed at 200 nm, and the ribbon width is adjusted by ±2 nm in 1 nm steps from 100 nm. The graphene carrier mobility and the graphene Fermi level are assumed to be 2271 cm^{-1} and -0.484 eV, respectively, where perfect absorption is achieved with a ribbon width of 100 nm. The peak frequency shifts by 13 cm^{-1} from 1350 cm^{-1} to 1363 cm^{-1}. The maximum average absorption is 95.2% at 1356 cm^{-1}.

4. Role of noble metal plasmonic structures

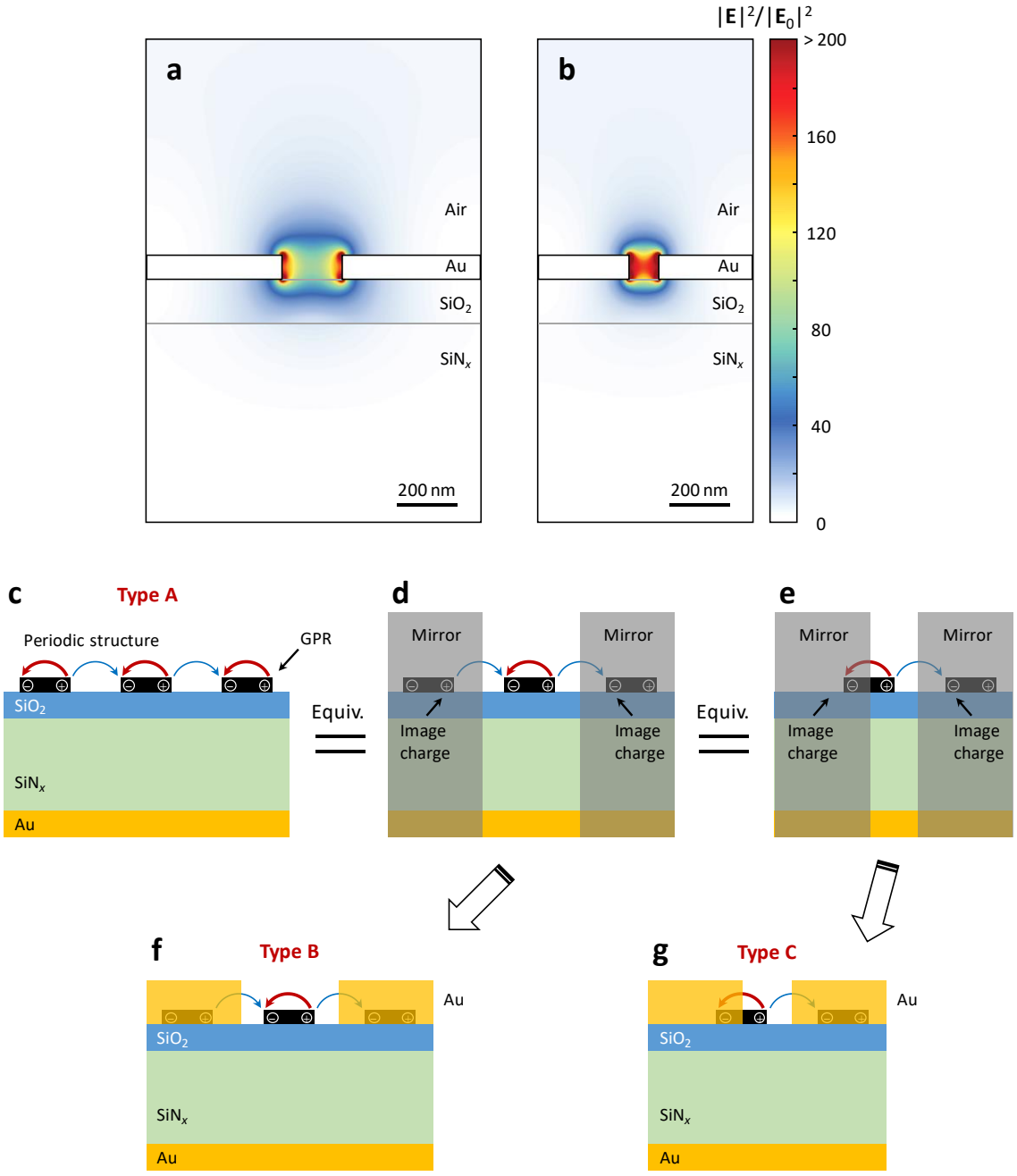

Figure S5. Electric intensity distributions without graphene plasmonic ribbons (GPRs) (a) in the type B structure and (b) in the type C structure exhibiting enhancement factors of 147 and 226, respectively. The field enhancement factors inside the metallic slits are calculated by averaging electric field intensity $|\mathbf{E}|^2/|\mathbf{E}_0|^2$ along the air/SiO_2 interface without intergap GPRs. (c) Schematic of charge distribution and induced electric field by graphene plasmons in the type A structure, and (d-g) equivalent schematic along with mirrors (or perfect electric conductor). Since the metallic strips in (f) and (g) efficiently reflect near-fields from the GPRs, we can consider the metal edges as mirrors similar to the perfect electric conductor boundaries constructing image GPRs.

5. Elemental absorption analysis

The elemental absorption values are obtained from full-wave simulations, using known complex refractive index values, and not from measurements. The absorption in the substrate includes the absorption of the SiO_2 layer, the SiN_x layer, and the back reflectors. The elemental absorption in each component can be evaluated by calculating the electric field intensity in a lossy medium. In the metal and dielectric layers, the elemental absorption is derived by $\frac{1}{P_0}\iint_A \frac{\omega\varepsilon_0}{2}\mathrm{imag}(\varepsilon_\mathrm{r})|\mathbf{E}|^2 dA$, where P_0 is the incident power per unit length, A is the area of the lossy medium, and ε_r is the relative permittivity of the lossy medium. Since the graphene is modelled by a sheet with zero thickness, the absorption in the graphene can be calculated by $\frac{1}{P_0}\int_{graphene}\frac{1}{2}\mathrm{real}(\sigma)|E_x|^2 dx$ assuming graphene is arranged along x-direction. Here, the frequency-dependent optical surface conductivity of graphene σ is calculated by the random phase approximation. In the local limit of the random phase approximation, neglecting spatial dispersion, the optical surface conductivity of graphene is given by $\sigma=\sigma_{\mathrm{intra}}+\sigma_{\mathrm{inter}}$, where σ_{intra} and σ_{inter} are the surface conductivities originating from the intraband and the interband transitions in graphene, respectively. Therefore, we can calculate the interband absorption and the plasmonic absorption in graphene by $\frac{1}{P_0}\int_{graphene}\frac{1}{2}\mathrm{real}(\sigma_{\mathrm{inter}})|E_x|^2 dx$ and $\frac{1}{P_0}\int_{graphene}\frac{1}{2}\mathrm{real}(\sigma_{\mathrm{intra}})|E_x|^2 dx$, respectively.

The absorption in the metallic strips is found to be small (<4%), as shown in the elemental absorption analysis (Figure S7). The metallic strips in the type B and C structures serve primarily to focus more light into the GPRs by the plasmonic antenna effect. For the free-space wavelength used in our experiments of ~7.37 μm, e.g., the geometrical resonances of metallic strips narrower than 1 μm, as in our type B and C structures, are in the infrared, far away from the strong intrinsic noble metal plasmonic resonance in the visible range. We note that despite operating at a wavelength far from the intrinsic noble metal plasmonic resonance, the metallic strips exhibit a strong plasmonic antenna effect at 7.37 μm.

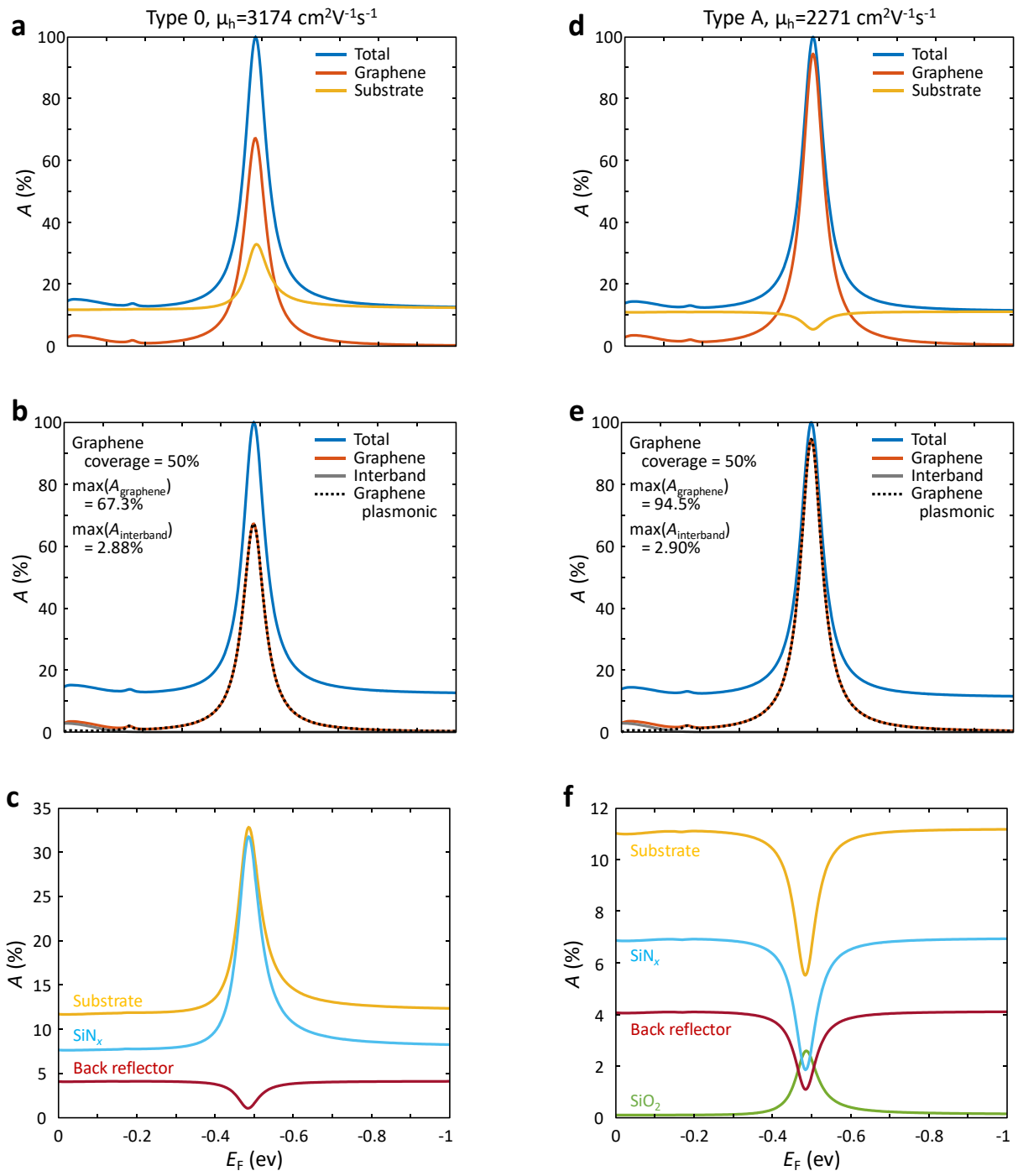

Figure S6. (a-c) Elemental absorption in the type 0 structure with the perfect absorption condition. (d-e) Elemental absorption in the type A structure with the perfect absorption condition. The absorption in the substrate indicates the combined absorptions in the SiO_2, SiN_x, and back reflector layers. The "Graphene", the "Interband", and the "Graphene plasmonic" in panels denote total absorption in graphene, absorption by interband transition in graphene, and absorption by graphene plasmonic resonance in graphene, respectively.

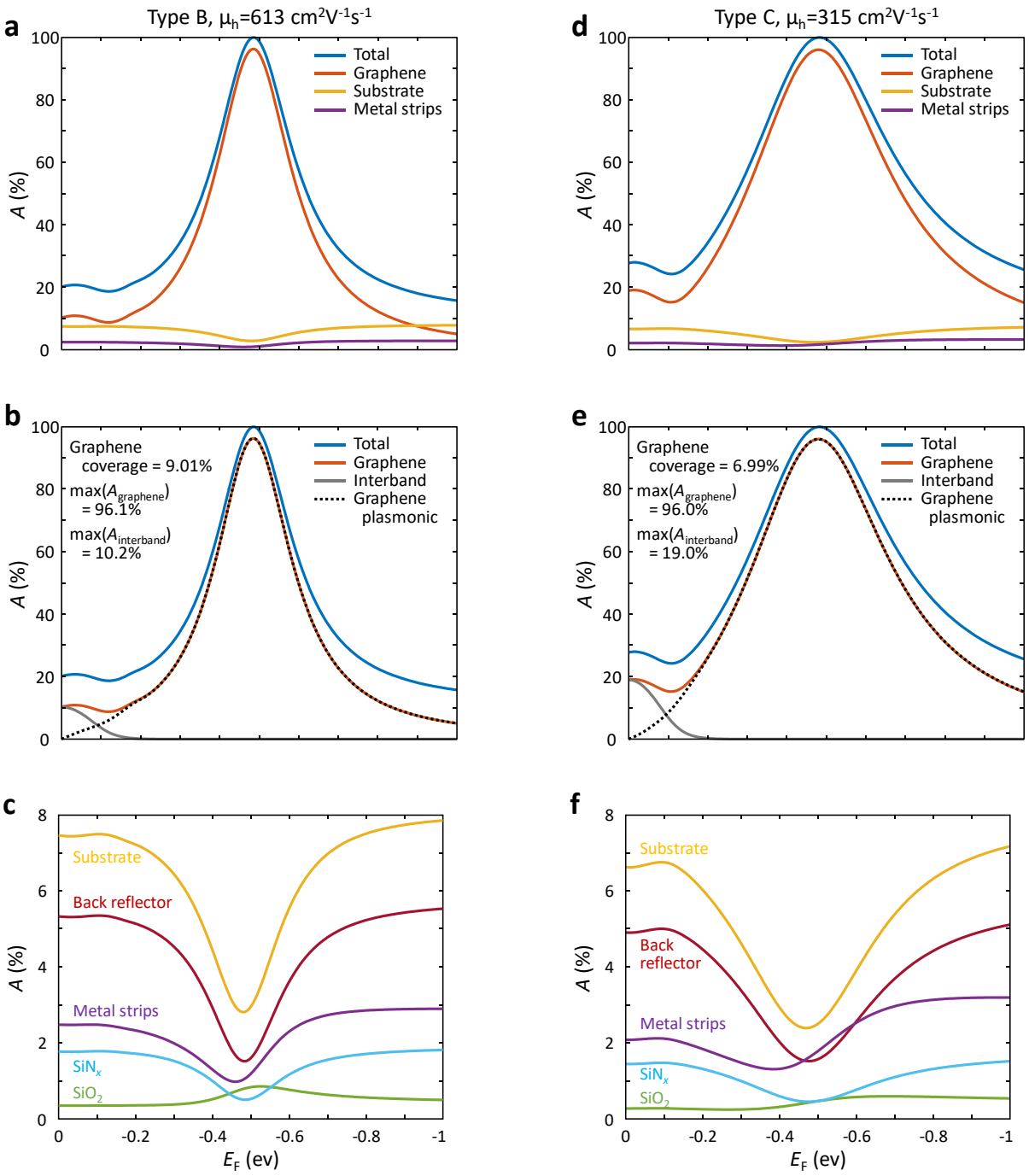

Figure S7. (a-c) Elemental absorption in the type B structure with the perfect absorption condition. (d-e) Elemental absorption in the type C structure with the perfect absorption condition. The absorption in the substrate indicates the combined absorptions in the SiO_2, SiN_x, and back reflector layers. The "Graphene", the "Interband", and the "Graphene plasmonic" in panels denote total absorption in graphene, absorption by interband transition in graphene, and absorption by graphene plasmonic resonance in graphene, respectively. The coupled noble metal plasmonic structures also increase the interband absorption in the graphene as well as the graphene plasmonic resonance.

6. Absorption maps

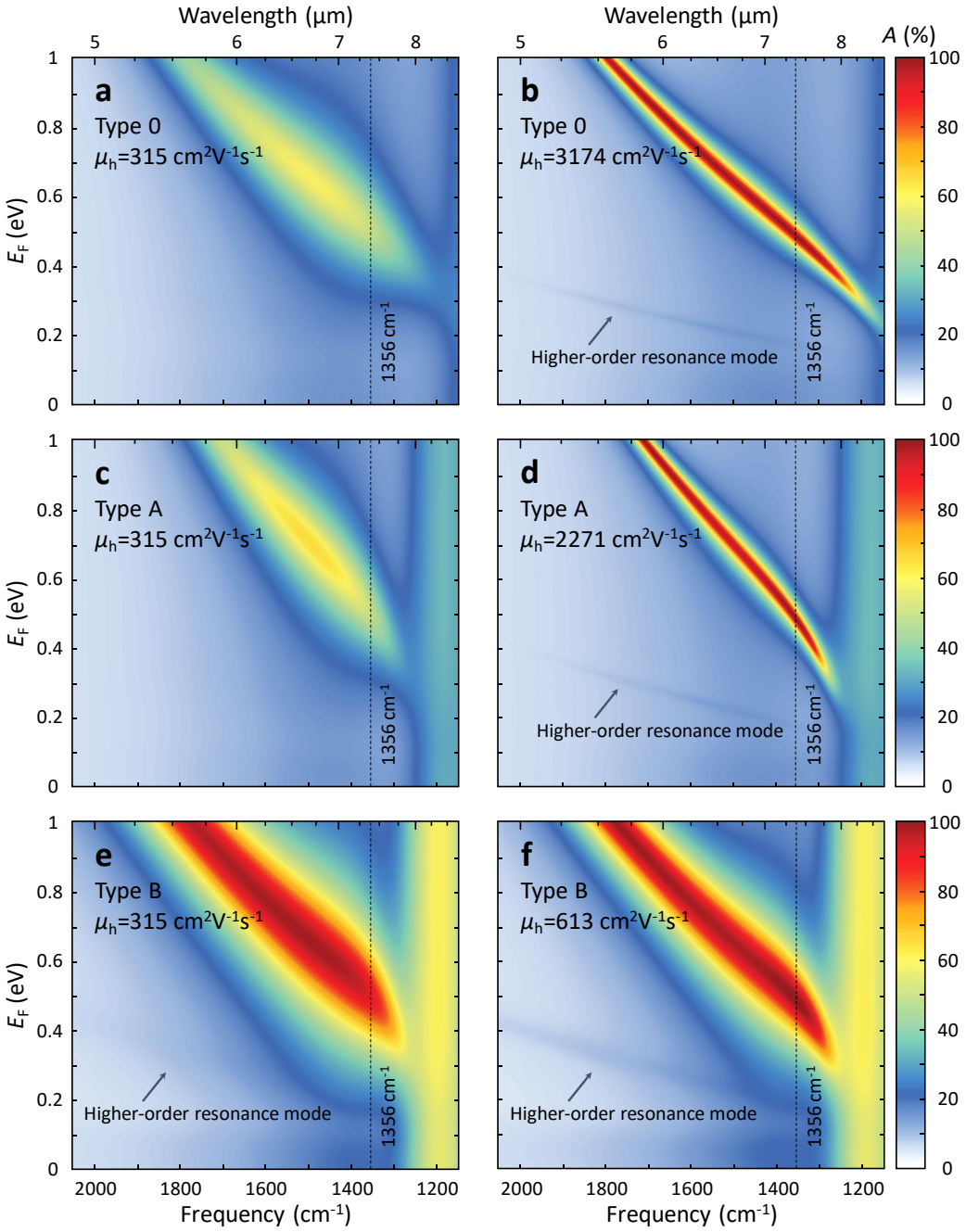

Figure S8. Absorption maps in the type 0 structure with (a) μ_h=315 $cm^2V^{-1}s^{-1}$ and (b) μ_h=3174 $cm^2V^{-1}s^{-1}$. Absorption maps in the type A structure with (c) μ_h=315 $cm^2V^{-1}s^{-1}$ and (d) μ_h=2271 $cm^2V^{-1}s^{-1}$. Absorption maps in the type B structure with (e) μ_h=315 $cm^2V^{-1}s^{-1}$ and (f) μ_h=613 $cm^2V^{-1}s^{-1}$.

7. Surface admittance model

Assuming that the graphene plasmonic nanostructure thickness is much thinner than free-space wavelength, the structure can be modeled by a thin screen located at z=0 with effective surface admittance Y_s as eq S2. By solving the boundary conditions in Figure S9a with eq S2, the effective surface admittance normalized by free-space admittance (Y_0) are derived as eqs S3 and S4 with the coefficients of eqs S5 and S6.

$$H_y(0^+) - H_y(0^-) = -Y_s E_x(0) \tag{S2}$$

$$\tilde{Y}_{s,r} = \frac{Y_{s,r}}{Y_0} = \frac{1 - r_0}{1 + r_0} - \frac{B_1}{A_1} \tag{S3}$$

$$\tilde{Y}_{s,t} = \frac{Y_{s,t}}{Y_0} = \frac{2}{A_1 t_0} - 1 - \frac{B_1}{A_1} \tag{S4}$$

$$A_1 = \cos(n_{SiO2} k_0 d_{SiO2}) - i \frac{n_{SiNx}}{n_{SiO2}} \sin(n_{SiO2} k_0 d_{SiO2}) \tag{S5}$$

$$B_1 = n_{SiNx} \cos(n_{SiO2} k_0 d_{SiO2}) - i n_{SiO2} \sin(n_{SiO2} k_0 d_{SiO2}) \tag{S6}$$

Here, $\tilde{Y}_{s,r}$ and $\tilde{Y}_{s,t}$ are normalized surface admittances calculated from the reflection coefficient (r_0) and the transmission coefficient (t_0), respectively, in Figure S9a.

In the type 0 and A structures, $\tilde{Y}_{s,r}$ and $\tilde{Y}_{s,t}$ are equal because eq S2 is the exact expression for the zero thickness of the structure. In the type B and C structures, however, $\tilde{Y}_{s,r}$ and $\tilde{Y}_{s,t}$ are different because light passing through the finite thickness graphene plasmonic nanostucture undergoes phase shift[9], as shown in Figure S9c,d. Therefore, we evaluated the normalized effective surface admittance by $\tilde{Y}_s = c_r \tilde{Y}_{s,r} + c_t \tilde{Y}_{s,t} + c_0$ to consider the phase shift through the finite thickness graphene plasmonic nanostucture. The fitting parameters c_r, c_t, and c_0 were determined by comparing full-wave simulations and results from eq S7. For the type B structure, the fitting parameters were c_r=0.923-i0.148, c_t=0.008+i0.053, and c_0=0.062-i0.224. For the type C structure, the fitting parameters were c_r=0.922-i0.142, c_t=0.013+i0.051, and c_0=0.057-i0.216. We expect that these fitting parameters are affected by the weak metal-insulator-metal plasmonic mode induced in the dielectric stack, which is not included in eq S7. When the SiN_x thickness is detuned from the critical thickness, a small deviation occurs in absorption between these models, as shown in Figure S13a,b. However, this deviation is very small, indicating that the graphene plasmonic resonances in the structures are dominant in the structures.

After obtaining the surface admittance from the semi-infinite substrate schematic, we can calculate the absorption of the structure by considering the interaction between the graphene plasmonic nanostructure and the Salisbury screen. By solving the boundary conditions outlined in Figure S9b, the reflection coefficient is derived as eq S7 with the coefficients of eqs S8-S11, and the absorption is 1-$|r|^2$ because there is no transmission.

$$r = -\frac{\tilde{Y}_s + \frac{C_2 + n_{Au} D_2}{A_2 + n_{Au} B_2} - 1}{\tilde{Y}_s + \frac{C_2 + n_{Au} D_2}{A_2 + n_{Au} B_2} + 1} = -\frac{\tilde{Y}_s + \tilde{Y}_{sub} - 1}{\tilde{Y}_s + \tilde{Y}_{sub} + 1} = -\frac{\tilde{Y}_L - 1}{\tilde{Y}_L + 1} \tag{S7}$$

$$A_2 = 1 - \frac{n_{SiNx}}{n_{SiO2}} \tan(n_{SiO2} k_0 d_{SiO2}) \cdot \tan(n_{SiNx} k_0 d_{SiNx}) \tag{S8}$$

$$B_2 = -\frac{i}{n_{\mathrm{SiO2}}}\tan(n_{\mathrm{SiO2}}k_0 d_{\mathrm{SiO2}}) - \frac{i}{n_{\mathrm{SiN}x}}\tan(n_{\mathrm{SiN}x}k_0 d_{\mathrm{SiN}x}) \quad \text{(S9)}$$

$$C_2 = -in_{\mathrm{SiO2}}\tan(n_{\mathrm{SiO2}}k_0 d_{\mathrm{SiO2}}) - in_{\mathrm{SiN}x}\tan(n_{\mathrm{SiN}x}k_0 d_{\mathrm{SiN}x}) \quad \text{(S10)}$$

$$D_2 = 1 - \frac{n_{\mathrm{SiO2}}}{n_{\mathrm{SiN}x}}\tan(n_{\mathrm{SiO2}}k_0 d_{\mathrm{SiO2}}) \cdot \tan(n_{\mathrm{SiN}x}k_0 d_{\mathrm{SiN}x}) \quad \text{(S11)}$$

As shown in eq S7, we can derive the substrate admittance $\tilde{Y}_{\mathrm{sub}}$ determined by the substrate parameters, and the condition of $\tilde{Y}_{\mathrm{s}} = 1 - \tilde{Y}_{\mathrm{sub}}$ achieves perfect absorption. In Figure S9-S12, the dotted black lines in the surface admittance charts correspond to the $1 - \tilde{Y}_{\mathrm{sub}}$ as a function of SiN_x thickness ($d_{\mathrm{SiN}x}$). This condition corresponds to the critical coupling induced by the interaction between the graphene plasmonic nanostructure and the substrate. Or, we can interpret the perfect absorption as an admittance matching condition between the air and the load admittance $\tilde{Y}_{\mathrm{L}}$, as shown in eq S7. The variation of absorptions for the type C structure calculate from eq S7 and full-wave simulations are compared in Figure S13, and they show good agreement.

To interpret the physical meaning of the surface admittance, we modified a susceptibility model for a dispersive material[10],

$$\tilde{Y}_{\mathrm{s}}(E_{\mathrm{F}}) = \tilde{Y}_{\mathrm{s},\infty} + i\tilde{\chi}(E_{\mathrm{F}}) = \tilde{Y}_{\mathrm{s},\infty} + i\tilde{\chi}_0 \frac{E_{\mathrm{F},0}/2}{(E_{\mathrm{F},0} - E_{\mathrm{F}}) + i\Delta E_{\mathrm{F}}/2} \quad \text{(S12)}$$

where $\tilde{Y}_{\mathrm{s}}$ is the surface admittance normalized by free-space admittance (Y_0) as a function of graphene Fermi level (E_{F}), $\tilde{Y}_{\mathrm{s},\infty}$ is the normalized surface admittance at a high graphene Fermi level limit similar to permittivity at high frequency in the Debye model[11], $\tilde{\chi}_0$ is the difference in the normalized surface admittance between low and high graphene Fermi levels, $E_{\mathrm{F},0}$ is the graphene Fermi level at a resonance, and ΔE_{F} is the linewidth in graphene Fermi level. In the resonant medium model[10], the real and imaginary part of the susceptibility are related to the refractive index of a medium and the absorption, respectively. Therefore, the surface admittance is multiplied by i to match the real and imaginary part of the resonant medium model with the surface conductance and surface susceptance of the graphene plasmonic nanostructure, respectively. We adopted $\tilde{\chi}(E_{\mathrm{F}})$ as a reduced susceptibility near resonance instead of a full susceptibility expression to account for the Lorentzian lineshape in the surface conductance from dipolar plasmonic resonance[10,12]. To include the net susceptance of the graphene plasmonic nanostructure dominated by noble metal plasmonic structures, $\tilde{Y}_{\mathrm{s},\infty}$ was taken at E_{F}=-20 eV. The surface admittances fitted by the modified susceptibility model for all structures are presented in Figure S10-S12 and Figure 3 of the manuscript.

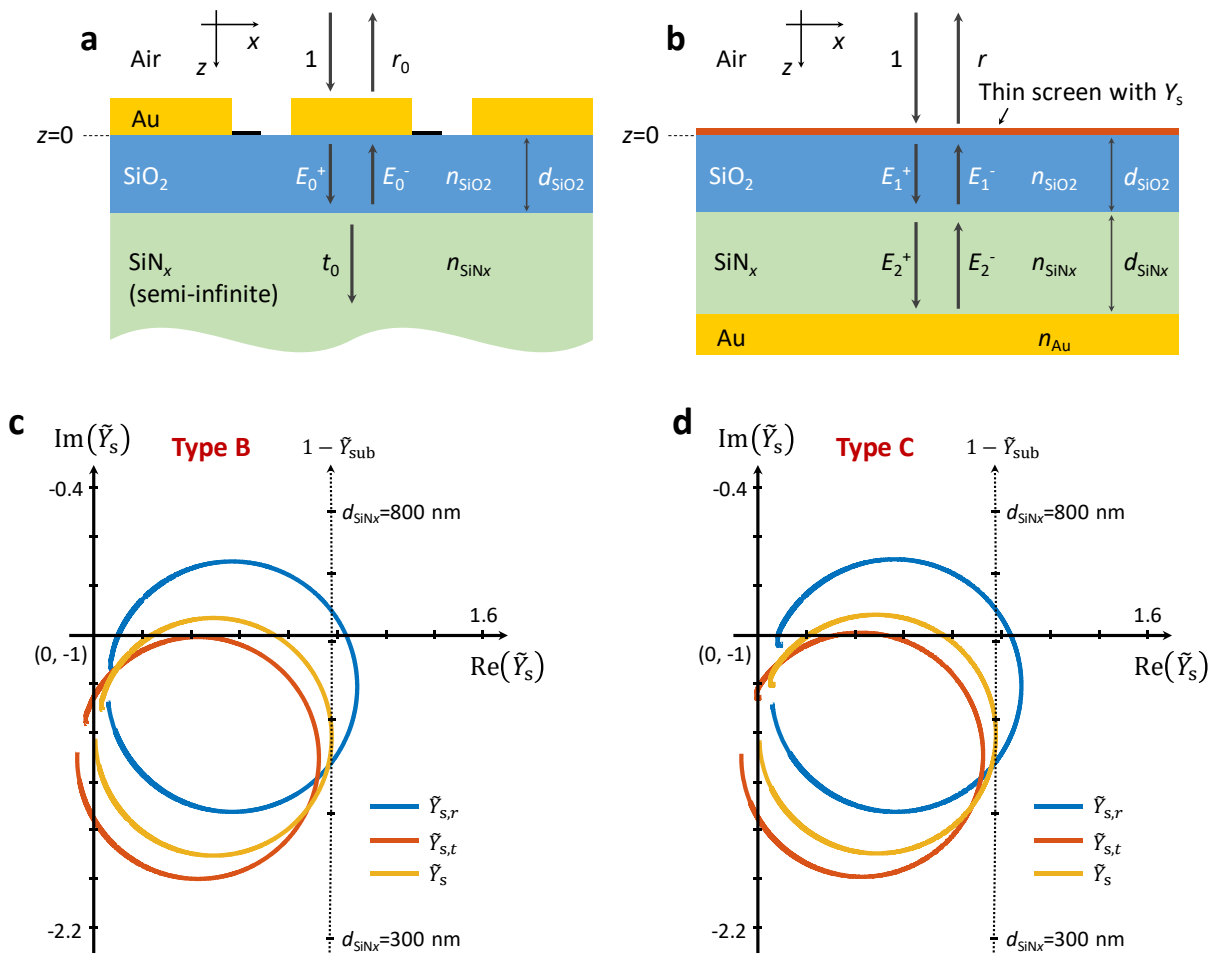

Figure S9. (a) Schematic of the structure consisting of graphene plasmonic ribbons coupled to sub-wavelength metallic slits, and (b) corresponding thin screen with effective surface admittance. Surface admittance charts of (c) the type B structure with μ_h=613 $cm^2V^{-1}s^{-1}$ and (d) the type C structure with μ_h=315 $cm^2V^{-1}s^{-1}$ showing the effect of the finite thickness structures. In (c) and (d), the graphene Fermi level varies from 0 eV to -20 eV, and the frequency is 1356 cm^{-1}.

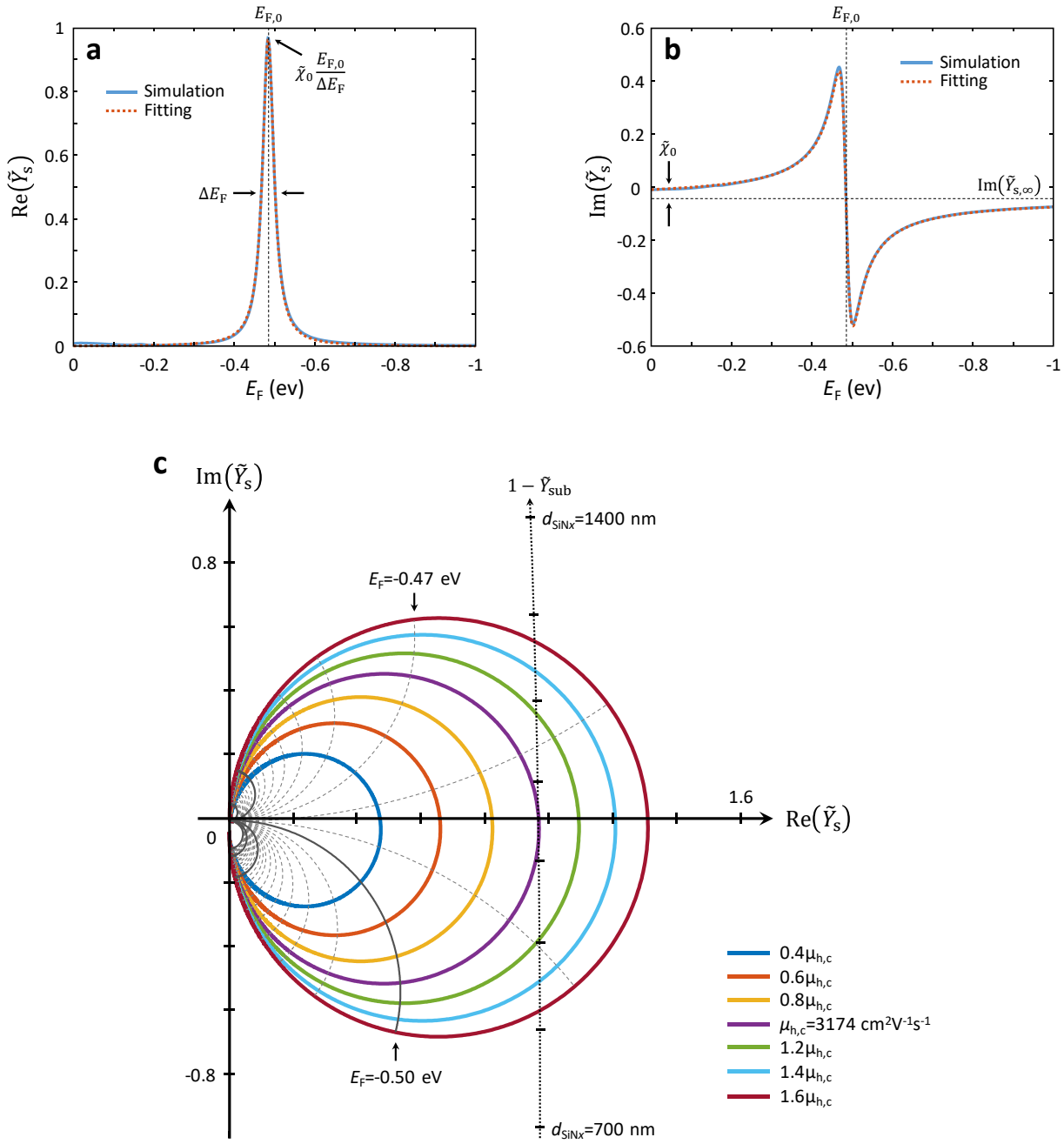

Figure S10. (a) The real part and (b) imaginary part of the surface admittance of the type 0 structure for the critical graphene hole mobility ($\mu_{h,c}$). The fitting parameters for the modified susceptibility model in eq S12 are $\tilde{Y}_{s,\infty}$=-0.043i, $\tilde{\chi}_0$=0.068, $E_{F,0}$=-0.485 eV, ΔE_F=0.034 eV. (c) Surface admittance chart of the type 0 structure at 1356 cm^{-1} with different graphene hole mobilities. The surface admittances are calculated from 0 eV to -20 eV of graphene Fermi level, and the equi-E_F lines from -0.3 eV to -0.8 eV with 0.01 eV steps (dotted grey lines) and 0.1 eV steps (solid grey lines). The frequency is 1356 cm^{-1} for all calculations.

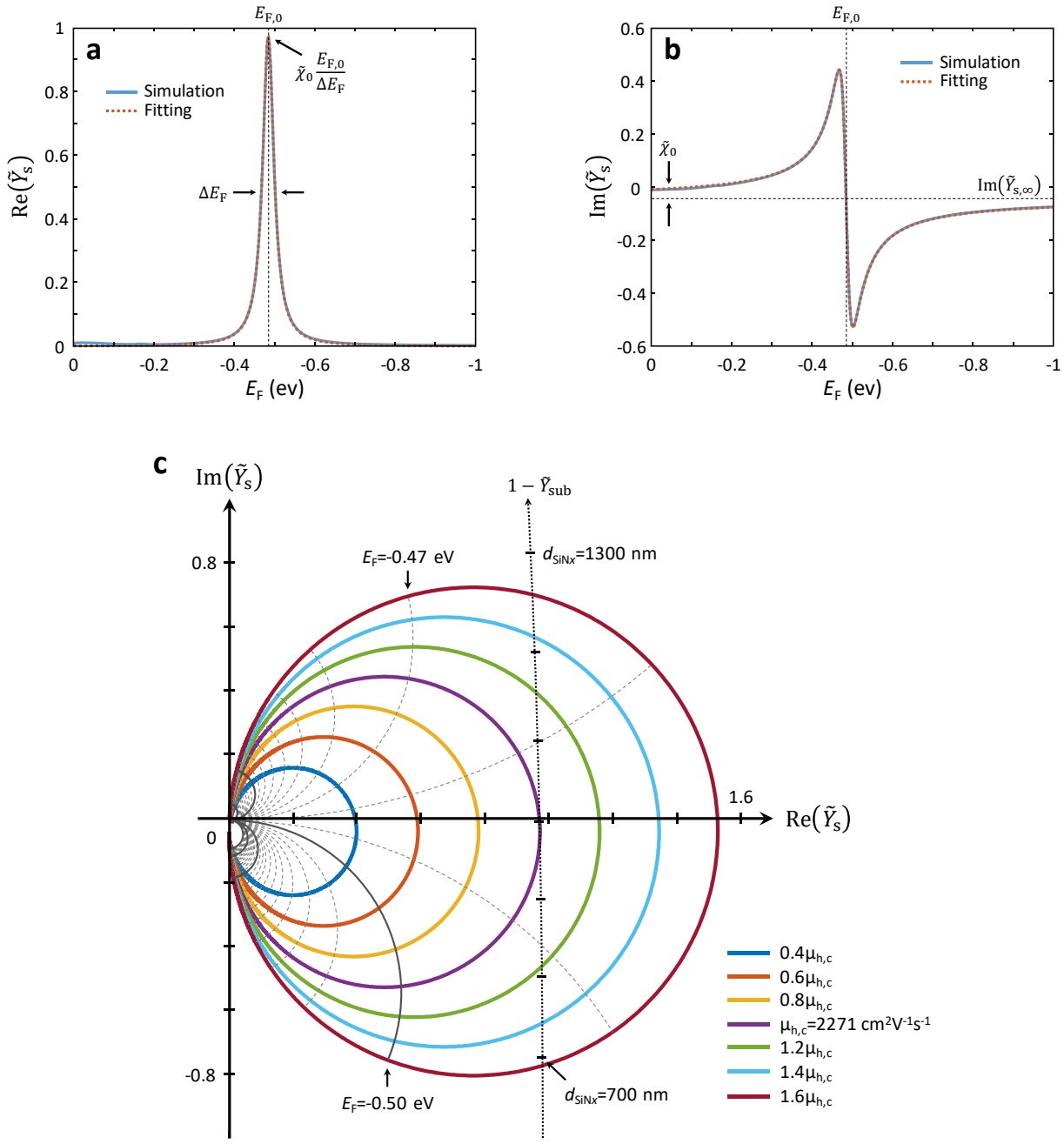

Figure S11. (a) The real part and (b) imaginary part of the surface admittance of the type A structure for the critical graphene hole mobility ($\mu_{h,c}$). The fitting parameters for the modified susceptibility model in eq S12 are $\tilde{Y}_{s,\infty}$=-0.043*i*, $\tilde{\chi}_0$=0.068, $E_{F,0}$=-0.485 eV, ΔE_F=0.034 eV. (c) Surface admittance chart of the type A structure at 1356 cm^{-1} with different graphene hole mobilities. The surface admittances are calculated from 0 eV to -20 eV of graphene Fermi level, and the equi-E_F lines from -0.3 eV to -0.8 eV with 0.01 eV steps (dotted grey lines) and 0.1 eV steps (solid grey lines). The frequency is 1356 cm^{-1} for all calculations.

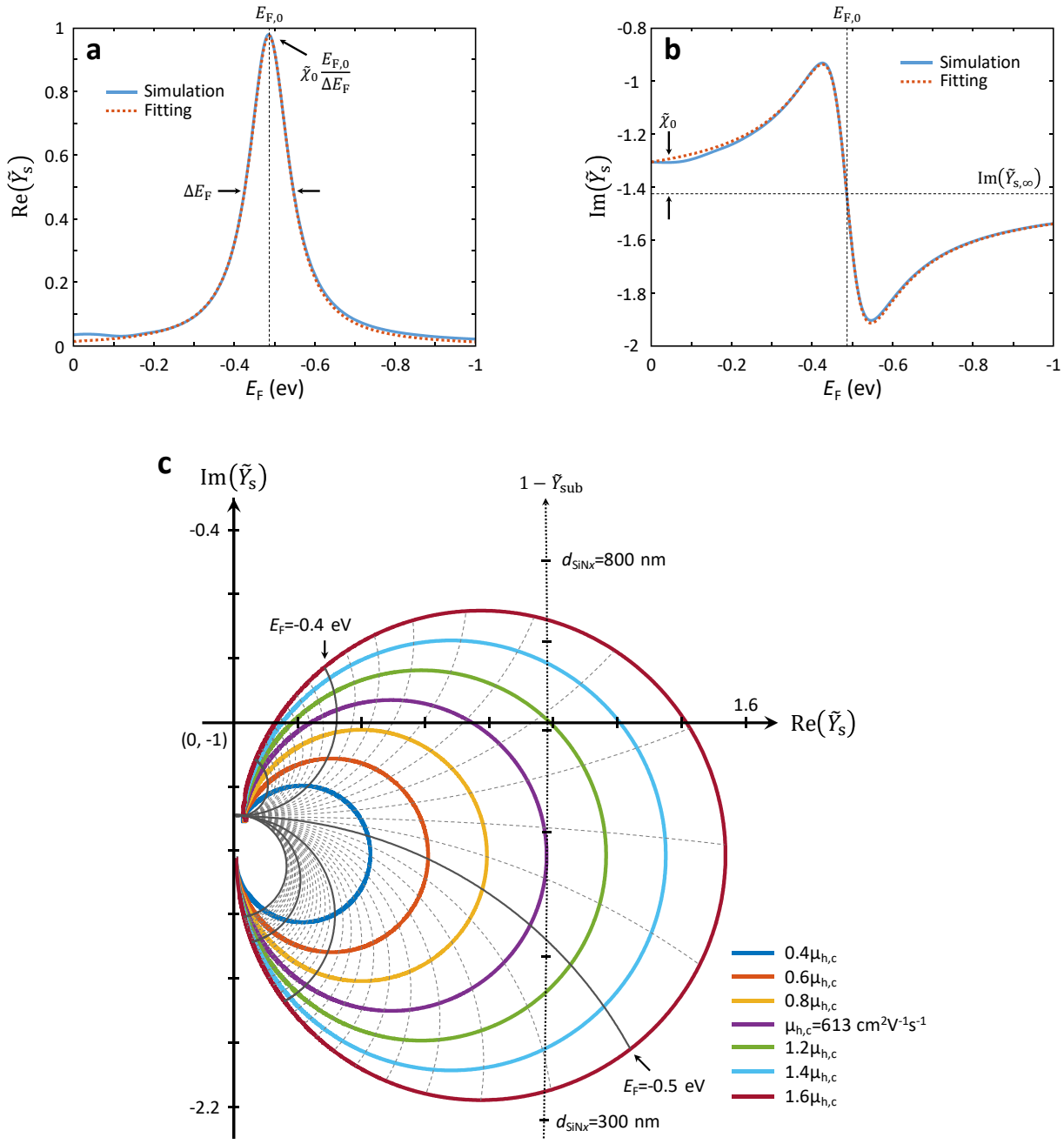

Figure S12. (a) The real part and (b) imaginary part of the surface admittance of the type B structure for the critical graphene hole mobility ($\mu_{h,c}$). The fitting parameters for the modified susceptibility model in eq S12 are $\tilde{Y}_{s,\infty}$=0.008-1.425i, $\tilde{\chi}_0$=0.243, $E_{F,0}$=-0.486 eV, ΔE_F=0.121 eV. (c) Surface admittance chart of the type B structure at 1356 cm^{-1} with different graphene hole mobilities. The surface admittances are calculated from 0 eV to -20 eV of graphene Fermi level, and the equi-E_F lines from -0.3 eV to -0.8 eV with 0.01 eV steps (dotted grey lines) and 0.1 eV steps (solid grey lines). The frequency is 1356 cm^{-1} for all calculations.

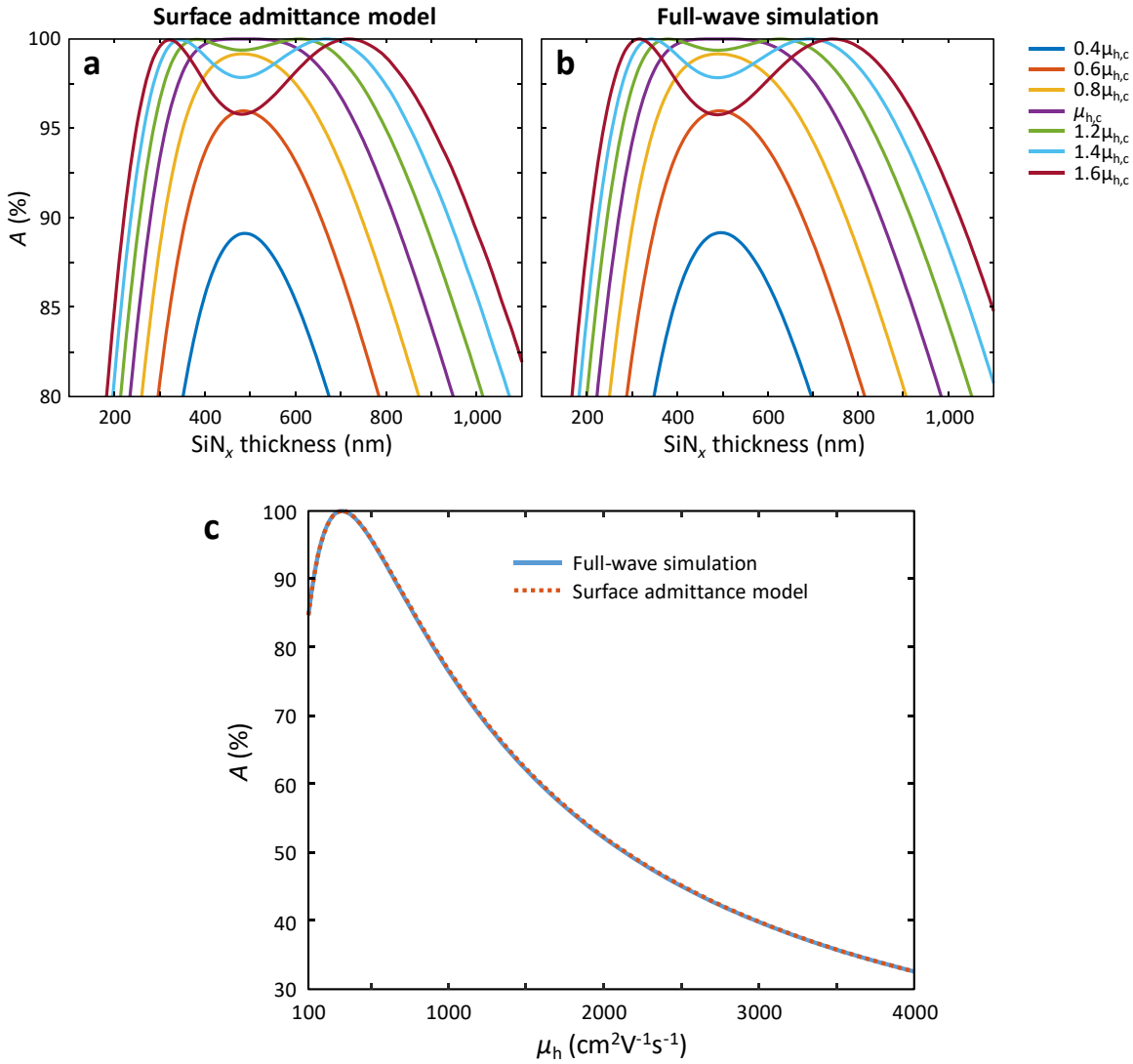

Figure S13. (a) The surface admittance model and (b) full-wave simulation with different graphene hole mobilities (μ_h) as a function of SiN_x thickness. The critical graphene hole mobility ($\mu_{h,c}$) is 315 $cm^2V^{-1}s^{-1}$. (c) Absorption as a function of graphene hole mobility (μ_h) calculated by full wave simulation and the surface admittance model.

8. Details on surface admittance

The critical line is defined by $1 - \tilde{Y}_{\mathrm{sub}}$, where $\tilde{Y}_{\mathrm{sub}}$ is normalized substrate admittance, and is a function of dielectric stack thickness. If there is zero absorption in a dielectric stack with a perfectly conducting back reflector, the Salisbury screen becomes lossless and the phase term varies depending on the dielectric stack thickness. Therefore, the real part of $\tilde{Y}_{\mathrm{sub}}$ (the substrate conductance) should always be zero independent of the dielectric stack thickness, and only the imaginary part of $\tilde{Y}_{\mathrm{sub}}$ (the substrate susceptance) depends on the dielectric stack thickness. This makes the critical line vertical in a surface admittance chart. In practice, there is small absorption in the SiO_2 and the SiN_x layers due to phonon modes, and Au back reflector is not a perfect conductor. These small absorptions lead to a small conductance in $\tilde{Y}_{\mathrm{sub}}$, resulting in a slight bending of the critical line and a small shift in the real part of $1 - \tilde{Y}_{\mathrm{sub}}$ away from one.

The surface conductance, or the real part of the surface admittance, can be a measure of the oscillator strength in the graphene plasmonic structure. As shown in the surface admittance charts, the maximum surface conductance strongly depends on the graphene hole mobility. This is mainly due to the fact that the higher graphene hole mobility leads to inducing stronger graphene plasmonic resonances in the graphene plasmonic nanostructures[13]. However, the stronger oscillator strength is not always preferable for achieving perfect absorption in the graphene plasmonic nanostructures. As described in the manuscript, the "optimum" oscillator strength exists to accomplish the critical coupling between the graphene plasmonic nanostructure and the Salisbury screen, or to match the load admittance to air. If the oscillator strength exceeds the optimum, the absorption becomes lower, and it is referred as over-coupling.

In a flat graphene sheet, the oscillator strength of graphene plasmonic resonance increases with higher graphene Fermi level because of larger amount of free carriers interacting with photons. However, there is also an optimum graphene Fermi level in the GPRs to achieve stronger resonance because we have to consider the Fabry-Perot resonance in the finite size resonators[2]. Therefore, the surface conductance is maximized at a certain graphene Fermi level, and it declines above the optimum graphene Fermi level, as shown in the surface admittance charts.

If the graphene hole mobility is larger than the critical graphene hole mobility, the $\mathrm{Re}(\tilde{Y}_{\mathrm{s}})$ exceeds one at the maximum resonance, which means the system is over-coupled to the free-space as its radiative damping rate is faster than its resistive damping rate[14]. Therefore, the resonance has to be detuned to lower the optical conductance in the graphene plasmonic nanostructure by adjusting the graphene Fermi level in order to satisfy the admittance matching condition. As we increase the graphene Fermi level from the resonance condition, the graphene plasmonic nanostructure begins to advance the phase of light, and similarly phase retardation occurs for lower doping level as shown in Figure 3b and Figure S12b. Consequently, as shown in Figure 3c and Figure S13a,b, the structure shows perfect absorption under two distinct admittance matching conditions: thinner substrate at high E_F, and thicker substrate at low E_F.

9. Optimization of structural design

By optimizing the sub-wavelength metallic slit structure, we can achieve perfect absorption in the graphene plasmonic nanostructure with even lower graphene hole mobility. Figure S14a,b shows the field enhancement factor inside the sub-wavelength metallic slits as a function of metallic strip width and metallic slit width, respectively. In Figure S14a, it is shown that wider metallic strip width enhances the field enhancement factor because of the increased cross-section capturing more light. The enhanced field enhancement leads to more optically conductive graphene plasmonic nanostructure, as shown in Figure S14c.

The narrower metallic slit also improves the field enhancement factor by squeezing more light, as shown in Figure S14b. In the 1:2 ratio of the GPR width and the metallic slit width, the narrower metallic slits reduces the GPR width, and it results in weakening the oscillator strength in the GPR. As a result, the optical conductance of the graphene plasmonic nanostructure decreases with the narrower metallic slit, as shown in Figure S14d. Although the wider metallic slit would be beneficial in terms of the optical conductance of the graphene plasmonic nanostructure, it requires higher graphene Fermi level, which could not be achievable by electrostatic gating.

Figure 4b of the manuscript shows perfect absorption at 1356 cm^{-1} in the optimized type C structure with the graphene hole mobility of 200 $cm^2V^{-1}s^{-1}$. The GPR width, the metallic slit width, the metallic strip width, the SiO_2 thickness, and the SiN_x thickness are 50 nm, 100 nm, 918 nm, 150 nm, and 295 nm, respectively. The perfect absorption is exhibited with the graphene Fermi level of -0.514 eV, and this range is achievable in an electrostatic gating method. Graphene nanoresonators cover 4.91% of the surface area, and the maximum absorption in the graphene is 94.3%. In addition, the interband absorption by the graphene in the optimized structure is higher than in other structures due to the enhanced light focusing effect despite lower graphene surface coverage ratio.

Compared to the other structures presented in the manuscript, the line shapes in graphene Fermi level are broader, as shown in Figure 4b of the manuscript. This broadening originates from the low Q-factor of the graphene plasmonic resonance with low graphene hole mobility[13]. Further improvement should be possible by tuning the metallic strip width and the dielectric stack thickness, and it allows for the perfect absorption even with lower graphene hole mobility.

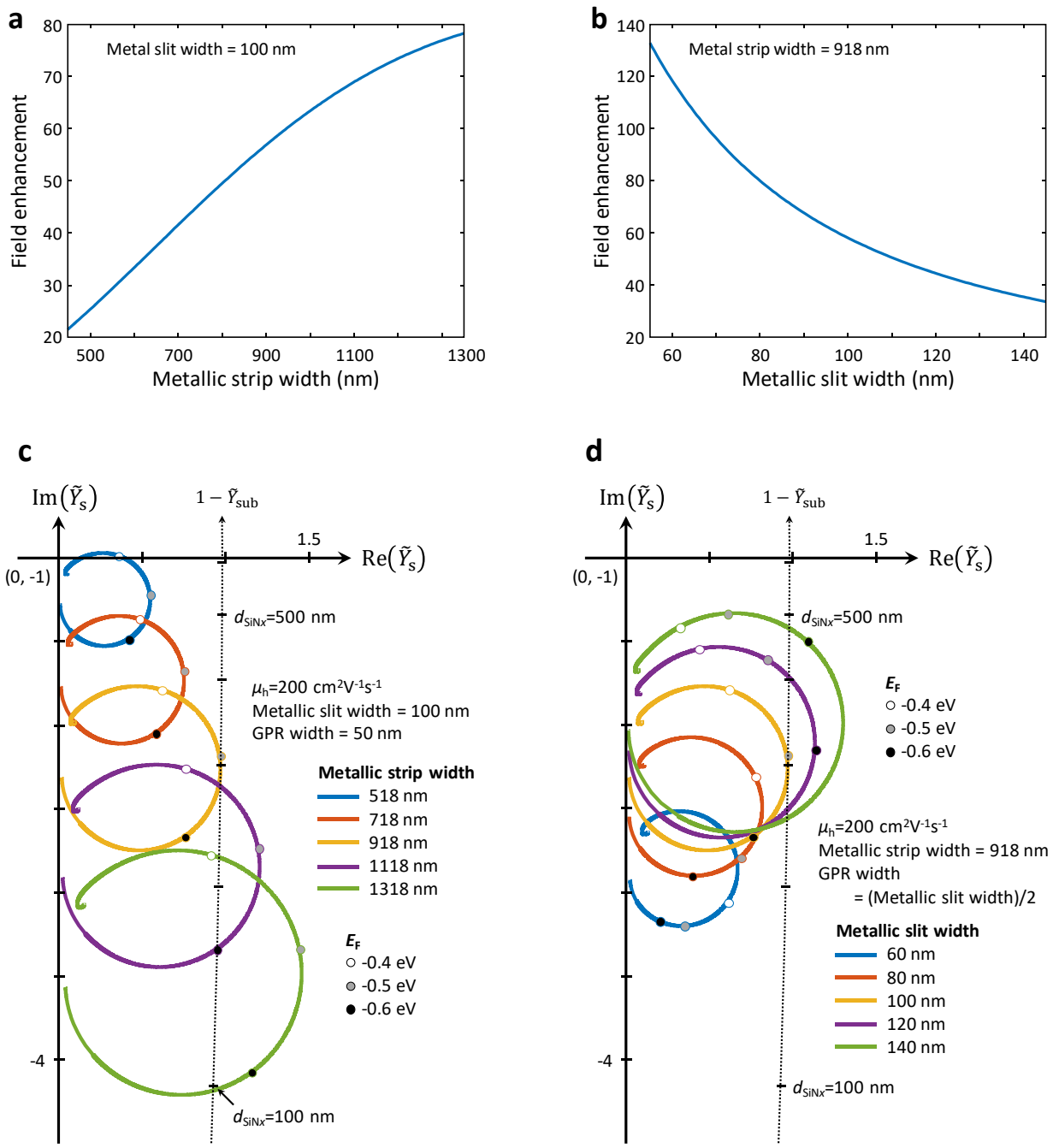

Figure S14. Field enhancement inside the sub-wavelength metallic slit on SiO_2 150 nm/semi-infinite SiN_x substrate without intergap GPRs and (a) as a function of metallic strip width and (b) as a function of metallic slit width. Surface admittance charts of the type C structure (c) with different metallic strip width and (d) with different metallic slit width. In (c) and (d), the graphene hole mobility is assumed to be 200 $cm^2V^{-1}s^{-1}$ for all calculations. The white, gray, and black dots in each surface admittance correspond to E_F=-0.4 eV, -0.5 eV, and -0.6 eV, respectively. The frequency is 1356 cm^{-1} for all calculations.

10. Characteristics of CVD-grown graphene and determination of graphene Fermi level

The Raman signal of the CVD-grown graphene was measured on a thermally grown SiO_2 substrate because of the strong photoluminescence emission of SiN_x over the visible range[15]. In Figure S15a, the *G*-peak and the 2*D*-peak are located at 1591 cm^{-1} and 2693 cm^{-1}, respectively, and their ratio of I_{2D}/I_G=2.82. The Raman spectrum shows that the *D*-peak (1350 cm^{-1}), which corresponds to defects in graphene, is very small, and the ratio of I_G/I_D=11.3.

The graphene Fermi level position is calculated using a capacitor model based on the graphene carrier density obtained from measurements of gate voltage-dependent resistance of the graphene[13,16]. Figure S15b shows the gate voltage-dependent resistance of the graphene exhibiting a charge neutral point at gate voltage V_g=261 V for the type A structure (SiO_2 150 nm/SiN_x 1 μm) and at gate voltage V_g=183 V for the type B and C structures (SiO_2 150nm / SiN_x 500 nm). In the capacitor model, the dielectric constants of SiO_2 and SiN_x were assumed as 5 and 10, respectively[2,13,17].

Figure S15c-e shows the graphene plasmon resonance frequencies of the type A, B, and C structures obtained by full-wave simulations and mid-infrared measurement results. In the type A structure, the -0.08 eV of offset gives better agreement between the simulation and the measurement results although good agreement is shown with less than 5% deviation without the offset. We expect that this offset originates from PMMA residue and trapped dopants beneath the graphene which induce local background doping in the GPRs of the type A structure[18,19]. In the type C structure, the measured graphene plasmonic resonance frequencies and the simulations are in good agreement below E_F=-0.53 eV, as shown in Figure S15e. However, the deviation between simulation and measurement increases above E_F=-0.53 eV, which we attribute to the pinning effect between the graphene/metal junctions[20] degrading the effective surface conductance at high frequencies, which result in suppression of the resonant absorption.

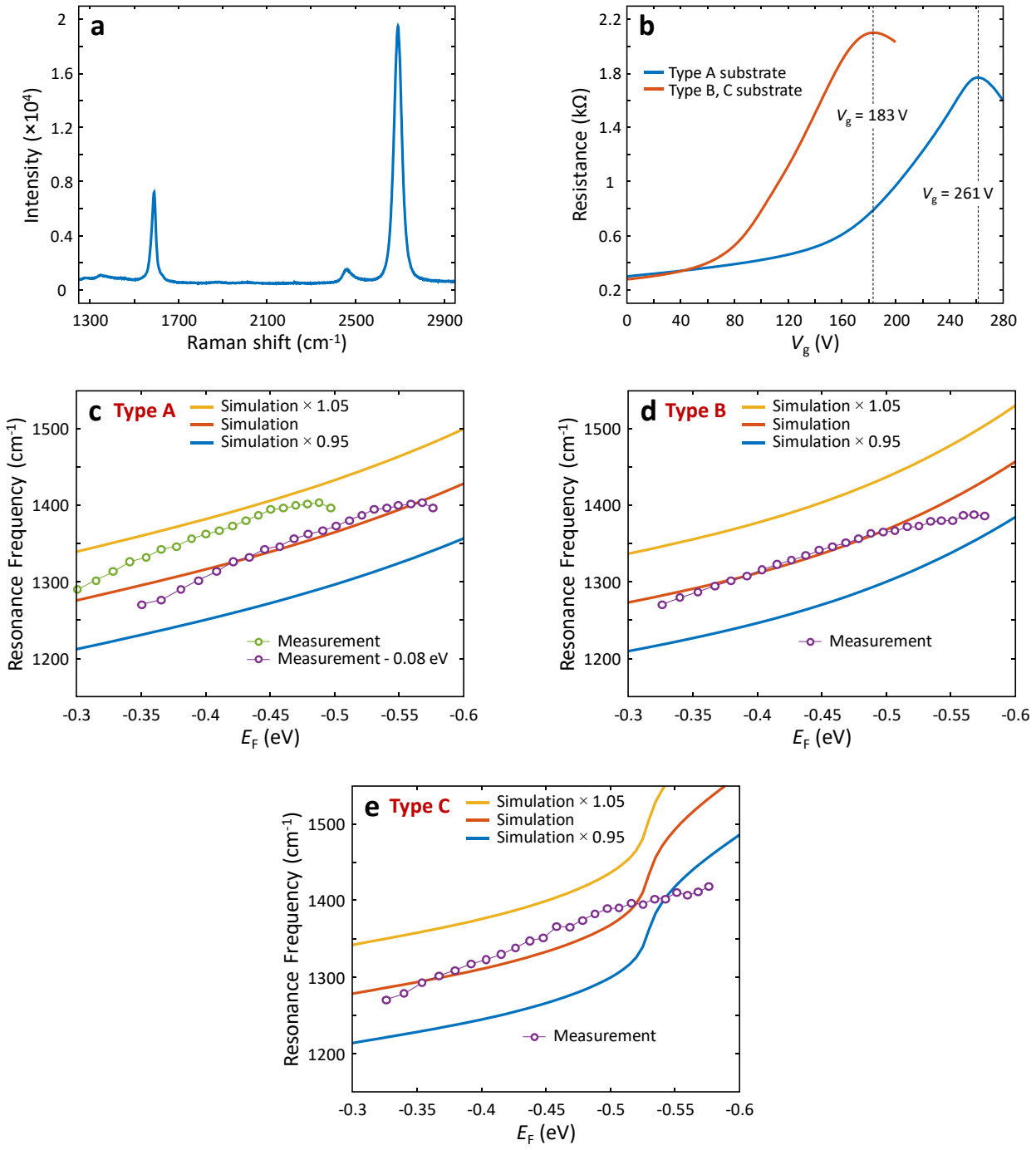

Figure S15. (a) Raman spectrum of graphene transferred onto thermally grown SiO_2 substrate, and (b) gate voltage-dependent resistance measurements of graphene on the SiO_2 150 nm /SiN_x 1 μm/Au substrate for the type A structure and the SiO_2 150 nm /SiN_x 500 nm/Au substrate for the type B and C structures, showing the charge neutral point at gate voltages of V_g=261 V and V_g=183 V, respectively. Graphene plasmon resonance frequency of (c-e) type A, B, and C structures, respectively, as a function of graphene Fermi level (E_F) for simulations and mid-infrared measurements. In **c**, the -0.08 eV of offset gives better agreement with simulation and measurement results.

11. Measured absorption and corresponding modulation efficiencies with an extended range of frequencies

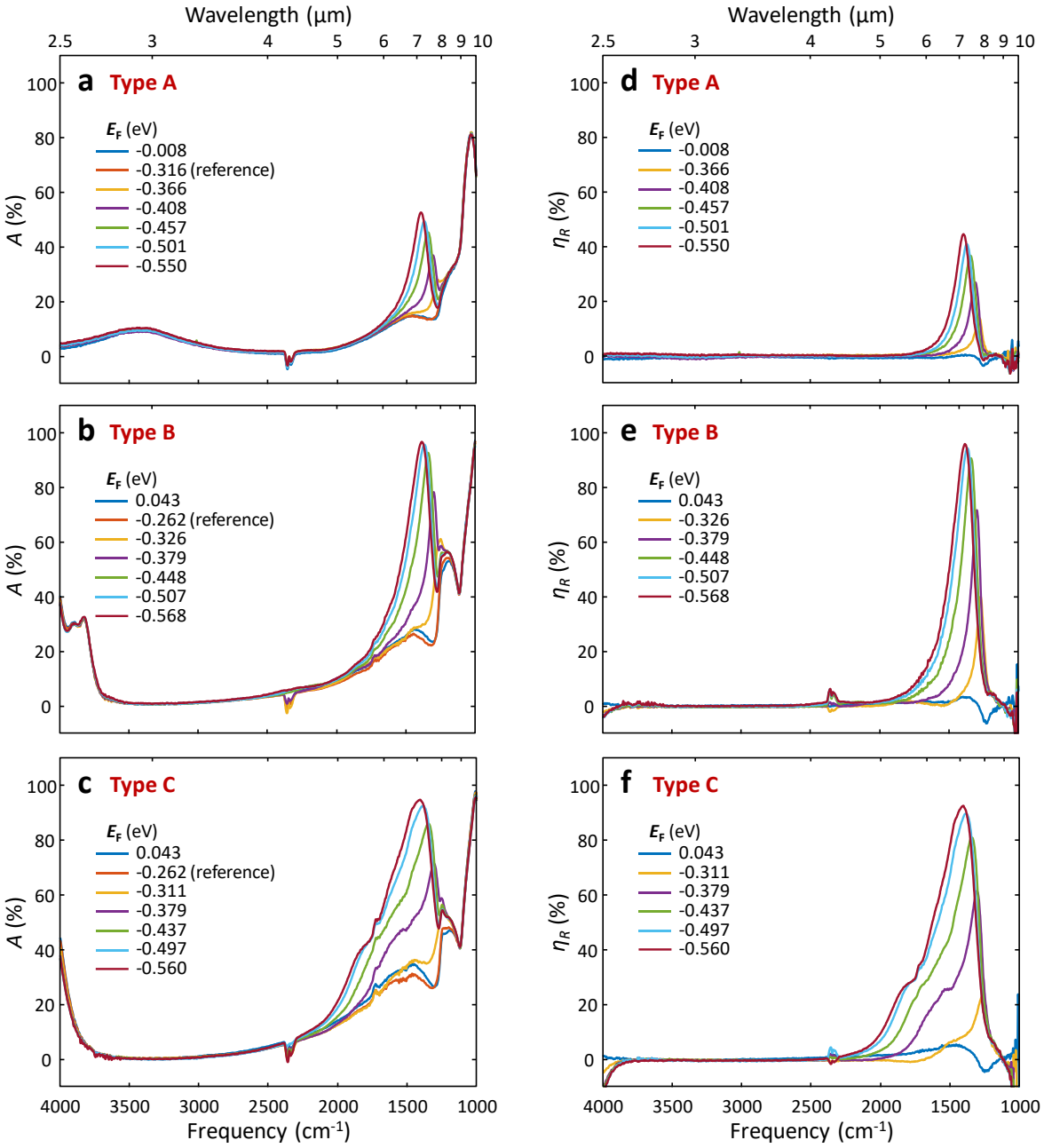

Figure S16. Measured absorption spectra and (d-f) corresponding modulation efficiency (η_R) of the type A, B, and C structures, respectively, for varying graphene Fermi level (E_F). The modulation efficiencies are calculated based on the reflection spectra with the graphene Fermi levels denoted by "reference". Small features at around 2350 cm^{-1} correspond to CO_2 absorption, which we expect was from a small amount of ambient air leaked into the FTIR microscope through a gap for electrical wires during measurement of background spectra and gate-dependent spectra.

12. Higher-order graphene plasmonic resonance mode

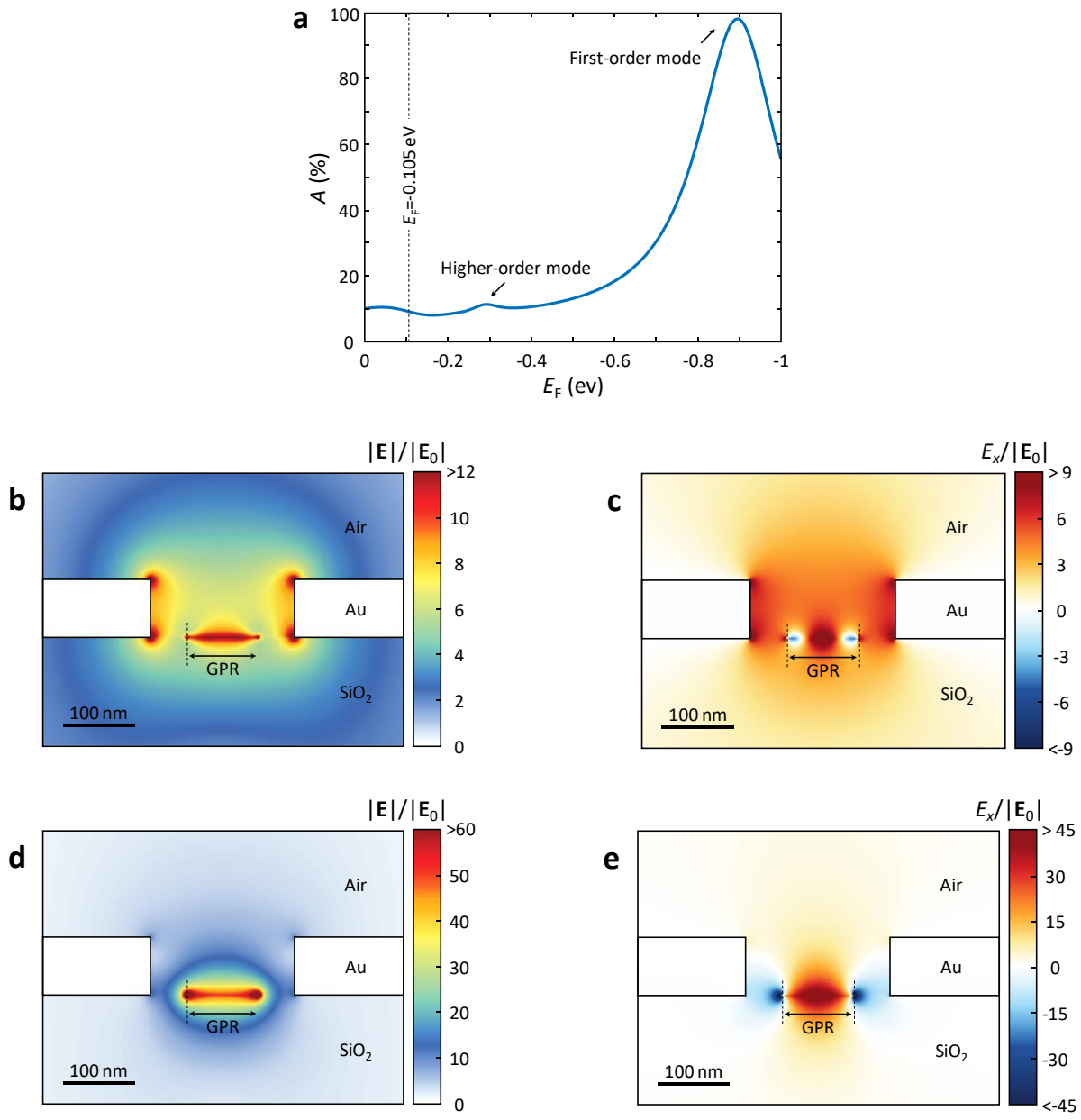

Figure S17. (a) Tunable absorption in the type B structure at 1700 cm^{-1} with μ_h=613 $cm^2V^{-1}s^{-1}$ as a function of graphene Fermi level (E_F). The absorption below E_F=-0.105 eV originates from the interband transition in graphene. The absorption peaks at E_F=-0.292 eV and E_F=-0.895 eV correspond to the higher-order and the first-order graphene plasmon resonance modes, respectively. (b) Electric field and (c) E_x distributions at E_F=-0.292 eV corresponding to the higher-order graphene plasmon resonance mode. (d) Electric field and (e) E_x distributions at E_F=-0.895 eV corresponding to the first-order graphene plasmon resonance mode.

13. Numerical fitting

Mid-infrared measurements demonstrate that low permittivity substrates and coupled sub-wavelength metallic slits play pivotal roles in enhancing the resonant absorption in GPRs. To analyze the measurement data, we adjusted the graphene hole mobilities in our simulations to match line shapes of the experimental modulation efficiency spectra, and the simulated maximum modulation efficiencies were fitted to the measured ones[13], as shown in Figure S18a-c. In the simulations, we also considered the finite numerical aperture (0.58) of the objective lens in the Fourier transform infrared measurements. Here, we expect that the estimated graphene hole mobility accounts mobility-limiting phenomena such as scattering from defects in graphene and edge roughness in the ribbons, and the scaling factor also accounts for a small fraction of electrically inactive resonators in the GPR arrays and finite numerical aperture effects on the measurement.

For the type A structure, the estimated graphene hole mobility was 420 $cm^2V^{-1}s^{-1}$, and the scaling factor was 0.752, as shown in Figure S18a. In the type B structure, the estimated graphene hole mobility of 500 $cm^2V^{-1}s^{-1}$ and the scaling factor of 0.963 show good agreement between the simulation and the measurement results, as shown in Figure S18b. In practice, the width of each GPR in an array may vary slightly from the average due to non-uniformities in pattern fabrication, and the spectra will thus exhibit inhomogeneous broadening arising from ensemble averaging. The type A structure has more GPRs than the type B structure per unit area, thus the ensemble averaging effect is expected to be more significant in the type A structure, broadening the spectral width of the collective graphene plasmonic resonances. In addition, the metallic strips present in the type B structure reduce the probability of electrical disconnections of the GPRs, increasing the scaling factor[13]. At the resonance frequencies exhibiting the highest absorption in each structure, the required graphene hole mobilities for perfect absorption are 1718 $cm^2V^{-1}s^{-1}$ and 521 $cm^2V^{-1}s^{-1}$ for the type A and B structures, respectively, as shown in Figure S18d. This indicates the interaction between the substrate and GPRs are in the under-coupled regime in the type A structure, and the type B structure is close to the critical coupling condition, which results in nearly perfect absorption in the latter.

Figure S18a,b shows that the fitting results in the type A and B structures match the measurement results very well. However, the measured modulation efficiency spectrum in the type C structure is narrower than the fitting results even with higher graphene hole mobilities as shown in Figure S18c. We expect that the narrower lineshape is due to a resonance frequency shift in the GPRs induced by the metallic strips. This effect likely originates from graphene Fermi level pinning that is known to occur at the graphene/metal junctions[20]. A non-uniform Fermi level along the GPRs in the vicinity of the metallic strips could degrade the effective surface conductance at high frequencies, leading to a suppression of resonant absorption. Similar behavior is also observed when fitting the graphene plasmon resonance frequency. As shown in Figure S15e, the measured graphene plasmon resonance frequencies are lower than those in simulations above E_F=-0.53 eV. Based on fitting results for the type A and B structures, the effective graphene hole mobility of the type C structure should be between 420 $cm^2V^{-1}s^{-1}$ and 500 $cm^2V^{-1}s^{-1}$, which are much higher than the μ_h=243 $cm^2V^{-1}s^{-1}$ required for perfect absorption in

the type C structure, as shown in Figure S18d. Therefore, the type C structure is expected to be in the over-coupled regime.

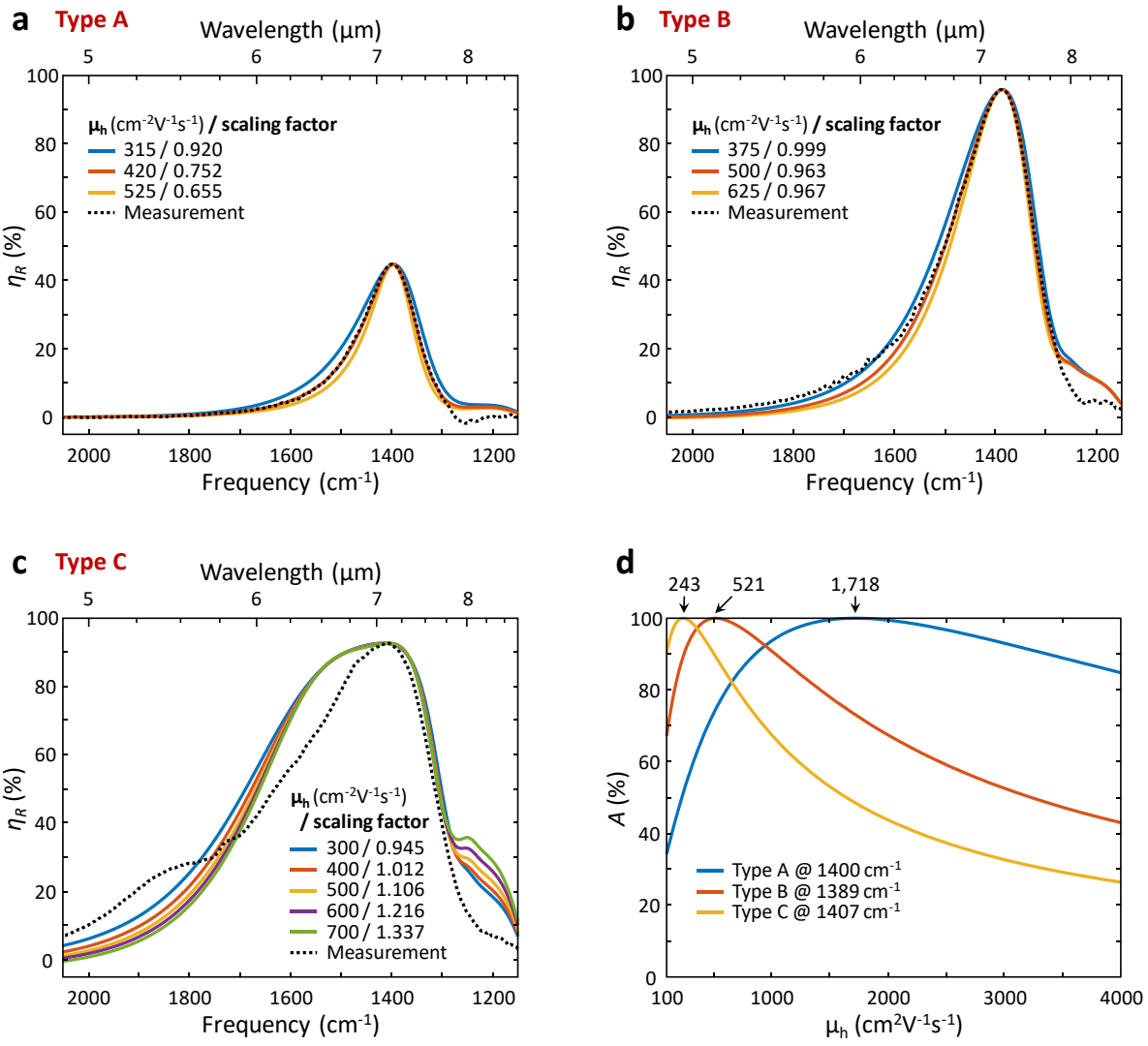

Figure S18. Numerical fitting results for modulation efficiencies in (a-c) type A, B, and C structures, respectively. The graphene hole mobilities and scaling factors for each structure are presented in the figure legends. (d) Absorption as a function of graphene hole mobility (μ_h) at the frequencies showing the maximum absorption in each structure. The required graphene hole mobilities for the type A, B, and C structures at their graphene plasmon resonance frequencies are 1718 $cm^2V^{-1}s^{-1}$, 521 $cm^2V^{-1}s^{-1}$, and 243 $cm^2V^{-1}s^{-1}$, respectively.

References

(1) Thongrattanasiri, S.; Koppens, F. H. L.; García de Abajo, F. J. *Phys. Rev. Lett.* **2012,** 108, 047401.

(2) Jang, M. S.; Brar, V. W.; Sherrott, M. C.; Lopez, J. J.; Kim, L.; Kim, S.; Choi, M.; Atwater, H. A. *Phys. Rev. B* **2014,** 90, 165409.

(3) Fante, R. L.; McCormack, M. T. *IEEE Trans. Antennas Propag.* **1988,** 36, 1443-1454.

(4) Jablan, M.; Buljan, H.; Soljacic, M. *Phys. Rev. B* **2009,** 80, 245435.

(5) Gan, C. H.; Chu, H. S.; Li, E. P. *Phys. Rev. B* **2012,** 85, 125431.

(6) Hwang, E. H.; Das Sarma, S. *Phys. Rev. B* **2007,** 75, 205418.

(7) Falkovsky, L. A. *J. Phys. Conf. Ser.* **2008,** 129, 012004.

(8) Falkovsky, L. A.; Varlamov, A. A. *Eur. Phys. J. B* **2007,** 56, 281-284.

(9) Yu, N. F.; Capasso, F. *Nat. Mater.* **2014,** 13, 139-150.

(10) Saleh, B. E. A.; Teich, M. C., *Fundamentals of photonics*. 2nd ed.; Wiley: Hoboken, N.J., 2007.

(11) Mantas, P. Q. *J. Eur. Ceram. Soc.* **1999,** 19, 2079-2086.

(12) Sönnichsen, C.; Franzl, T.; Wilk, T.; von Plessen, G.; Feldmann, J. *New J. Phys.* **2002,** 4, 93.1-93.8.

(13) Kim, S.; Jang, M. S.; Brar, V. W.; Tolstova, Y.; Mauser, K. W.; Atwater, H. A. *Nat. Commun.* **2016,** 7, 12323.

(14) Wu, C. H.; Neuner, B.; Shvets, G.; John, J.; Milder, A.; Zollars, B.; Savoy, S. *Phys. Rev. B* **2011,** 84, 075102.

(15) Kistner, J.; Chen, X.; Weng, Y.; Strunk, H. P.; Schubert, M. B.; Werner, J. H. *J. Appl. Phys.* **2011,** 110.

(16) Das, A.; Pisana, S.; Chakraborty, B.; Piscanec, S.; Saha, S. K.; Waghmare, U. V.; Novoselov, K. S.; Krishnamurthy, H. R.; Geim, A. K.; Ferrari, A. C.; Sood, A. K. *Nat. Nanotechnol.* **2008,** 3, 210-215.

(17) Schwartz, G. C.; Huang, Y. S.; Patrick, W. J. *J. Electrochem. Soc.* **1992,** 139, L118-L122.

(18) Pirkle, A.; Chan, J.; Venugopal, A.; Hinojos, D.; Magnuson, C. W.; McDonnell, S.; Colombo, L.; Vogel, E. M.; Ruoff, R. S.; Wallace, R. M. *Appl. Phys. Lett.* **2011,** 99, 122108.

(19) Chan, J.; Venugopal, A.; Pirkle, A.; McDonnell, S.; Hinojos, D.; Magnuson, C. W.; Ruoff, R. S.; Colombo, L.; Wallace, R. M.; Vogel, E. M. *ACS Nano* **2012,** 6, 3224-3229.

(20) Khomyakov, P. A.; Starikov, A. A.; Brocks, G.; Kelly, P. J. *Phys. Rev. B* **2010,** 82, 115437.